Stony Brook University

Determination of the Monoclinic Properties of Human Tooth Enamel Microstructure by a Periodic Three Dimensional Finite Element Model

A Thesis Presented

by

Cunyou Lu

to

The Graduate School

in Partial Fulfillment of the

Requirements

for the Degree of

Master of Science

in

Mechanical Engineering

Stony Brook University

December 2010

Stony Brook University

The Graduate School

Cunyou Lu

We, the thesis committee for the above candidate for the
Master of Science degree, hereby recommend
acceptance of this thesis.

Dr. Chad Korach, Thesis Co-Advisor
Assistant Professor in Mechanical Engineering

Dr. Toshio Nakamura, Thesis Co-Advisor
Professor in Mechanical Engineering

Dr. Oscar Lopez-Pamies, Chairperson of Defense
Assistant Professor in Mechanical Engineering

Dr. Mark Wolff, Outside Member
Professor in College of Dentistry, New York University

This thesis is accepted by the Graduate School

Lawrence Martin
Dean of the Graduate School

Abstract of the Thesis

Determination of the Monoclinic Properties of Human Tooth Enamel Microstructure by a Periodic Three Dimensional Finite Element Model

by

Cunyou Lu

Master of Science

in

Mechanical Engineering

Stony Brook University

2010

Researchers have reported diverse mechanical properties (Young's modulus) of human tooth enamel from experiments and finite element simulations, because of the complicated microstructure, which contains variations in crystal orientations and non-homogeneous properties. Although past models have effectively considered the microstructural effects, appropriate conditions for introducing crystal orientations within enamel rods and the property variations between rods and the interrod enamel are still necessary.

In this thesis, the micromechanical response of the enamel microstructure is investigated using a periodic finite element model to determine the effective monoclinic mechanical properties and determine localized effects of microstructure on the stress field. A spherical micro-indentation test was conducted on the bulk enamel model and the effective homogeneous model. The difference in response to indentation loading between the heterogeneous and homogeneous models revealed changes related to the enamel microstructure.

The model can be used to consider changes in effective properties of enamel based on microstructural variations, which can be applied to restorative materials attached or embedded within enamel. The study of the influence of microstructure on the damage generation and failure modes of enamel can also be accomplished using the model, which may be due to fractures and the abrasion-erosion wear process.

Dedicated to my wife.

Table of Contents

List of Figures

List of Tables

Acknowledgements

I would like to take this opportunity thank all the people who helped me over my research work.

First of all, I'd like to thank my co-advisors, Prof. Chad Korach and Prof. Toshio Nakamura, for their assistance and invaluable support throughout my thesis work. Prof. Korach's wisdom, patience and advices have been important to me. It's been a great learning experience working under his mentorship. Prof. Nakamura has guided me through the finite element modeling methods, for which I appreciated. I have learned useful techniques of numerical analysis from him. I could not have finished my thesis without the great support of my co-advisors.

Also I want to thank Prof. Oscar Lopez-Pamies for agreeing to be my thesis committee chairperson and Prof. Mark Wolff from New York University for being my committee member.

I would like to thank all my lab mates for their support on my projects. Dr. Wei Zhao provided AFAM test results for comparison and also helpful discussions about my model. Changhong Cao helped me prepare my samples. And all of them gave great suggestions on my presentations and poster.

It's been a great pleasure to work on my thesis with so many clever minds. They were always willing to help with my problems. I really enjoyed working with my co-advisors Prof. Korach and Prof. Nakamura. I could not say thanks enough for their support.

Chapter 1 Introduction

Teeth serve an indispensible role in people's daily life in several aspects, for instance the mastication process. An introduction of the structure of human teeth is presented offering an overview of the subject building to a detailed discussion of enamel.

1.1 Human Tooth Structure

Large physical forces, estimated as 300 N (Fernandes, Glantz et al. 2003) and large contact stress which can reach 2.5 GPa (Hayasaki, Okamoto et al. 2004) may occur during the mastication process; therefore the human tooth must be mechanically capable to fulfill this function in an oral environment.

Structurally the tooth consists of hard, inert and acellular enamel accommodating the hardness, supported by a more resilient but less mineralized connective hard tissue in dentin which surrounds the dental pulp (see Figure1.1). This highly mineralized protective layer of enamel functions as a shield providing hardness and toughness to withstand masticating forces.

Only a limited succession of teeth occur in humans where newly generated teeth are larger in size due to the growth of the face and jaws. After the succession, the teeth become permanent and generally non-regenerative.

1.2 Enamel

Human tooth enamel is the outer layer of the tooth which protects dentin and the nerves from mechanical and chemical impact. As shown in Figure1.1, the cross-sectional thickness varies from less than 1mm (in the crown-root junction) to around 2.5 mm (in the crown surface). Enamel has evolved to specifically function as a load-bearing, erosion and abrasion-resistant protective coating with properties that develop due to the extremely high percentage of mineral content and unique microstructure.

Enamel is the most highly calcified tissue in the human body, and consists approximately of an inorganic mineral content (96%) and organic matter (4%) by weight (Avery, Steele et al. 2002). The inorganic component is a crystalline hydroxylapatite (HAp). The organic matrix consists of only non-collagenous proteins which likely do not take major responsibilities of structural function. The almost total absence of protein matrix leads to two major issues of enamel: first, a high percentage of mineral increases hardness of enamel tremendously but also makes enamel brittle; second, the lack of proteins makes the enamel incapable of self-regenerating.

Despite the importance of enamel for the function of human teeth, enamel is not regenerative due to the mechanism of its formation. The cells called ameloblasts, which is responsible in formation of enamel, are lost upon the end of enamel maturation (Nanci and Ten Cate 2008). Thus the enamel becomes dead tissue, and cannot be regenerated once failure occurs.

1.2.1 Microstructure

The primary structural unit of enamel is called a prism with specific mineral crystal orientations, and a sheath region which is mainly organic. The acid etched surfaces of enamel are shown in Figure 1.2 and Figure 1.3 for the longitudinal and transverse view of prisms. Generally the prism grows perpendicular to the surface of dentin thus they can bear extremely large normal loads during masticating process by transferring high loads into the softer dentin tissue. The size of a single prism is approximately 7 μm × 5 μm according to the atomic force microscopy image in Figure 1.4.

The transverse contour of the prisms is shaped like a key-hole with a large circular head and a thin tail, periodically repeating in the cross-sectional plane (see Figure 1.5). The prism

consists of highly organized and packed hydroxyapatite (HAp) with specific crystal orientations shown as dark lines in Figure 1.5, and an organic matrix of proteins surrounding the HAp crystals with thickness of 2 nm (Jeng, Lin et al. 2009). The HAp crystals have cross-sectional dimensions of 68 nm by 26 nm (Kerebel, Daculsi et al. 1979) and are believed to be over 100 μm in length, even as long as the thickness of enamel (Daculsi, Menanteau et al. 1984; Nanci and Ten Cate 2008). The long axes of the HAp crystal composites run in the general direction of the longitudinal axis of the prism in the head part and rotate in a perpendicular direction to the prism in the tail region. The calcium phosphate that comprises HAp contains a hexagonal crystal structure, and results in a hexagonal shaped cross-sectional profile of the crystal, though this becomes distorted due to compaction (Nanci and Ten Cate 2008).

1.2.2 Hydroxyapatite

Hydroxyapatite (HAp) is a natural form of calcium phosphate salt in the form of $Ca_5(PO_4)_3(OH)$ or more often presented as $Ca_{10}(PO_4)_6(OH)_2$ since it indicates the conceptual entity with a least amount of ions. Some substitution may occur by fluoride, chloride or carbonate. It crystallizes in the hexagonal crystal system. Besides enamel, up to 45% of bone is made up of a modified form of hydroxylapatite (Norman, Vashishth et al. 1995).

Young's modulus of HAp is has been measured as 110-135 GPa (Katz and Ukraincik 1971; Katz 1985; Weiner and Wagner 1998; Viswanath, Raghavan et al. 2007) and is generally treated as an isotropic material (Spears 1997; White, Luo et al. 2001; Shimizu, Macho et al. 2005; Xie, Swain et al. 2009). According to White, enamel is 3 times tougher than geologic HAp but geologic HAp is much harder than enamel, demonstrating that the inclusion of the

protein matrix and the unique structural organization of HAp and protein within enamel provide the difference in the mechanical properties of enamel from that of HAp.

1.2.3 Enamel proteins

The main components of the proteins surrounding HAp crystals are noncollagenous proteins such as amelogenins, enamelin and ameloblastin (Nanci and Ten Cate 2008). In the modeling of enamel, there have been different values of the protein modulus used in past work. In Spears and Mishizu's work, a value of 4.3 GPa for the young's modulus of keratin was assigned as the elastic modulus of the enamel proteins, assuming an isotropic material behavior, while Xie at el have utilized a much smaller value of 0.1 GPa in their work. Unfortunately, no direct measurement of the elastic modulus of enamel proteins has been reported.

1.3 Significance

The study of mechanical properties of enamel based on its microstructure can provide valuable insights into many aspects, such as mechanisms of wear processes, effects of erosion, and the development of restorative materials that imitate the structure and properties of natural enamel.

The effective mechanical properties (Young's modulus) of human tooth enamel have been studied through experiments and finite element simulations, because of the complicated microstructure, which contains variations in crystal orientations and non-homogeneous properties. The orientation was taken into consideration later in many microscopic tests such as nanoindentation tests, but appropriate conditions for introducing crystal orientations within enamel rods and the property variations between rods and interrods are yet to be considered.

The investigation of the micromechanical response of enamel rods through finite element modeling using a periodic model is presented in this work to determine the effective mechanical

properties for enamel as a monoclinic material, and to determine the effects of microstructure on the stress field. Simulation of a spherical indentation in the longitudinal direction of an enamel bulk model is also investigated to study the microstructural response during indentation. Spherical indentation simulates the natural loading of enamel, thus provides a response related to its normal function.

The model developed in this work has a direct application to dental science. Variations in the local enamel properties due to disease, age, environment, or ultrastructural changes can be utilized to determine the microscale or bulk properties of enamel. This can aid in predictive capabilities for dental restorations and surface treatments of enamel.

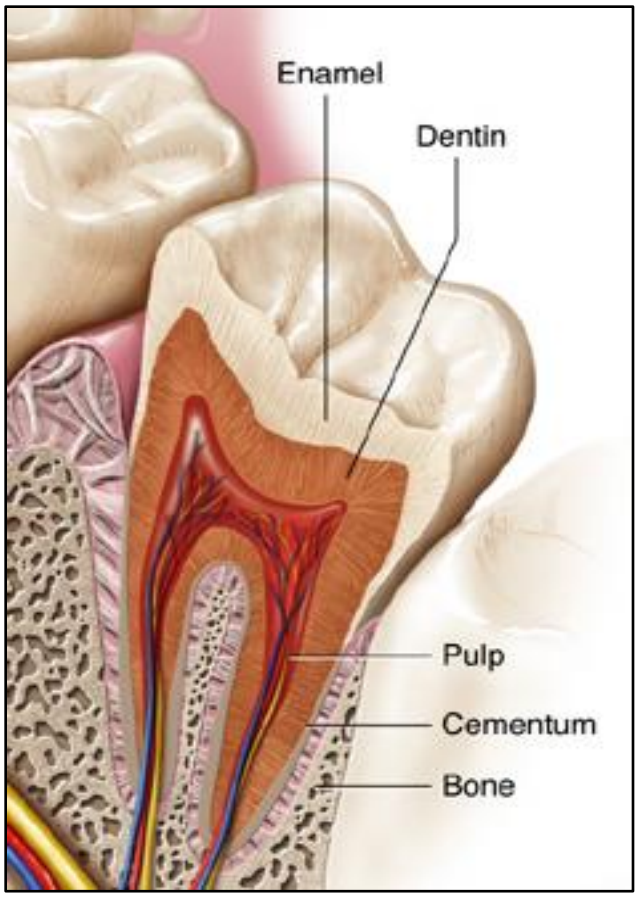

Figure1.1 Illustration of tooth structure (Nanci and Ten Cate 2008)

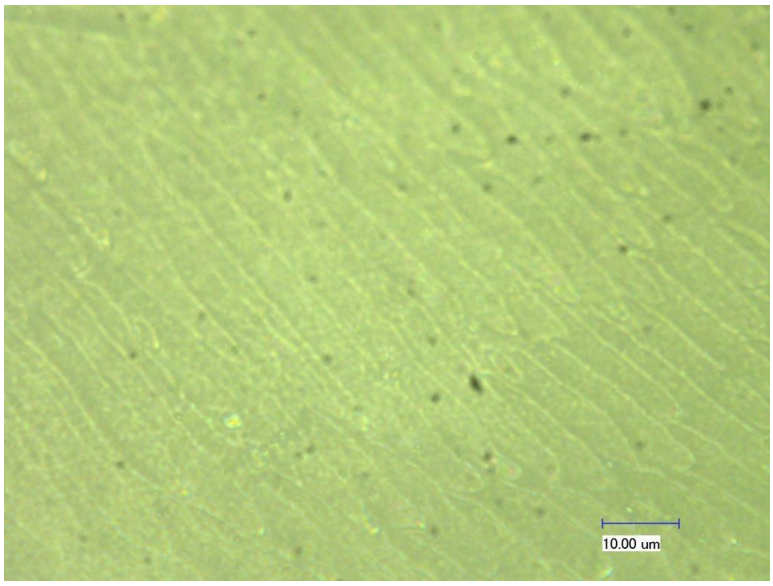

Figure 1.2 Optical image of enamel microstructure (axial cross-sectional view) after acid etching

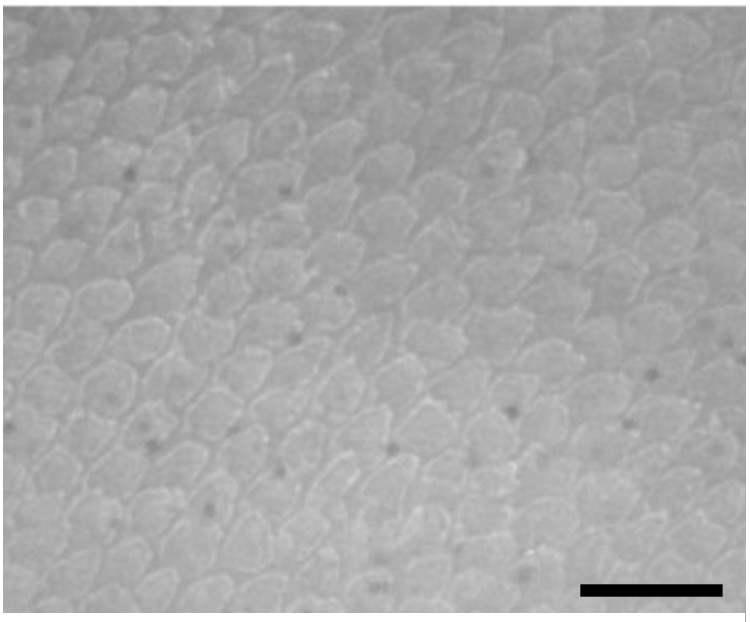

Figure 1.3 Optical image of enamel microstructure (occlusal view) after acid etching

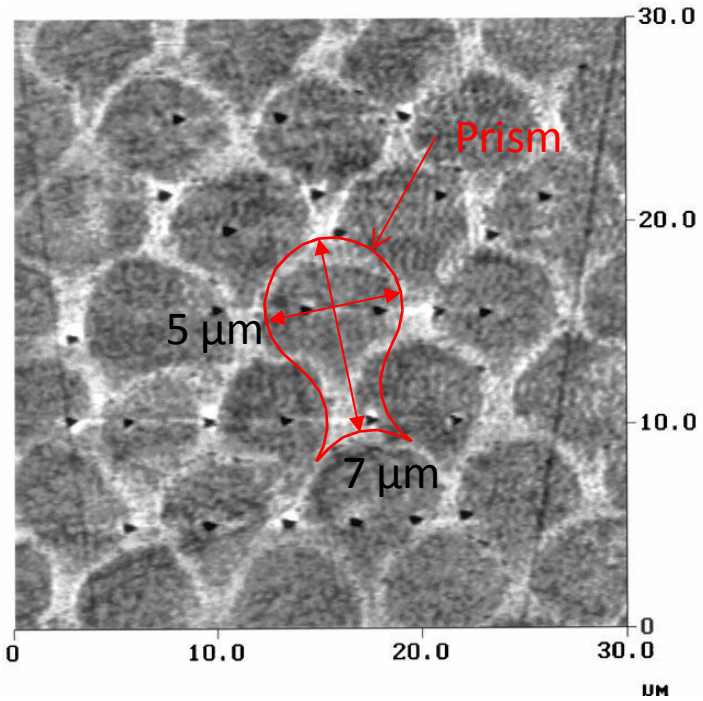

Figure 1.4 AFM image showing the rod arrangement in occlusal section (Habelitz, Marshall et al. 2001)

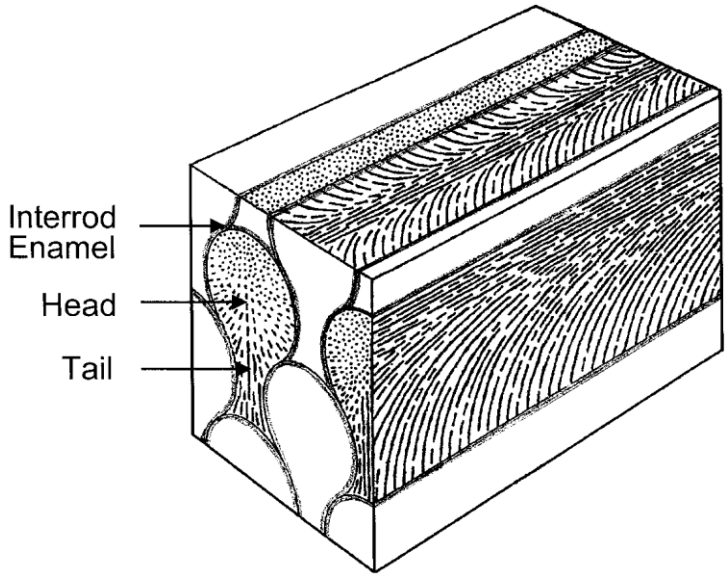

Figure 1.5 Schematic illustration of enamel microstructure showing alignment of highly packed fiber-shaped HAp (Meckel, Griebstein et al. 1965)

Chapter 2 Modeling of Enamel Mechanical Properties

The objective of the mechanical modeling is to develop a global constitutive relationship of enamel, i.e. stress-strain relationship. This is achieved using a linear elastic finite element model of the enamel microstructure. Detailed information of the microstructural modeling is described in this chapter.

2.1 Meshing

The first step in building the finite element model of enamel is to understand the fundamental repeating shape of the structure and create a mesh that can be utilized in the modeling. As shown in Figure 2.1, four identical circles that represent the enamel rods with the same diameter of 5 μm were drawn next to each other so their centers would form a square with edge length equal to 5 μm. Utilizing the region inside the four circles in conjunction with the topmost circle in Figure 2.1, the contours of a keyhole-shaped rod and interrod tail with dimensions of 5 μm wide by 7 μm long, which are approximately the dimensions of an enamel rod, were obtained. These keyhole-shaped rods can be reproduced in the same routine of drawing identical circles in a plane. Extrusion of the two-dimensional contours along the normal direction of the surface creates a three-dimensional model of an enamel rod, and completes the representation of the repeated keyhole structure.

When conducting the meshing of the enamel rod, the configuration of the outer and inner layers was considered in advance for assigning changes in the material orientation in different locations. Each square in Figure 2.1 represents one brick element with uniform properties, which is the basic unit of the finite element calculation. Additional consideration was drawn when breaking the outer contour into discrete straight lines since the discrete contour has to coincide with itself when shifted in plane.

2.2 Representative unit cell

The meshing of the rod is carefully designed so that a representative unit cell (RUC) model is established. A RUC is a small material region that can structurally represent the entire material by repeating itself infinitely. It can be regarded as an initiating unit of known repeating material structure. A unit-cell model is an effective approach frequently used when predicting material behavior in the case where the material contains repeated structure in certain patterns.

In this case, the smallest RUC for enamel could be a single rod. But it would be complicated to interpret average stress and strain over the keyhole shape, and difficult to implement. Instead, a square domain with four corners at near centers of the rod heads was chosen as shown in Figure 2.2, which is exactly equivalent to double the surface area of a single rod. The height extruded along the out of plane direction was chosen to be equal to the length of the square domain so a uniform cube was obtained to simplify calculation.

When the periodic unit cell is introduced to study the bulk properties of the material, appropriate periodic boundary conditions must be prescribed on the unit cell in order to represent the bulk properties in a limited microstructure. The details will be addressed in the periodic boundary condition section.

The RUC model is the dominate model utilized in this work. It contains 240 three-dimensional (3D) elastic brick elements and 546 nodes. The model is adequate and time-efficient to model the mechanical response of a heterogeneous material and linking the microstructure with the global properties.

2.3 Local element properties:

Locally, the enamel prisms are composed of inorganic mineral-hydroxyapatite and organic matrix- proteins with specific orientations. The structure of the hydroxyapatite-protein

matrix is similar to that of a fiber reinforced composite, which is axisymmetric in the long direction as shown in Figure 2.3. It is suitable to treat the local properties as transversely isotropic. The local properties of the elements are modeled as transversely isotropic (with 5 material constants) and variable orientations of the HAp crystal composite with the elements

The governing equation for a transversely isotropic material is:

$$\begin{pmatrix} \varepsilon_{11} \\ \varepsilon_{22} \\ \varepsilon_{33} \\ \gamma_{23} \\ \gamma_{31} \\ \gamma_{12} \end{pmatrix} = \begin{pmatrix} 1/E_L & -\nu_{LT}/E_L & -\nu_{LT}/E_L & 0 & 0 & 0 \\ -\nu_{LT}/E_L & 1/E_T & -\nu_{TT}/E_T & 0 & 0 & 0 \\ -\nu_{LT}/E_L & -\nu_{TT}/E_T & 1/E_T & 0 & 0 & 0 \\ 0 & 0 & 0 & 1/\mu_{TT} & 0 & 0 \\ 0 & 0 & 0 & 0 & 1/\mu_{LT} & 0 \\ 0 & 0 & 0 & 0 & 0 & 1/\mu_{LT} \end{pmatrix} \begin{pmatrix} \sigma_{11} \\ \sigma_{22} \\ \sigma_{33} \\ \tau_{23} \\ \tau_{31} \\ \tau_{12} \end{pmatrix} \quad (2.1)$$

In the equation, five constants are listed to define the elastic behavior of the transversely isotropic material: E_L , E_T , ν_{LT} , ν_{TT} and μ_{LT}, where E_L and E_T are the Young's moduli with respect to the longitudinal direction and transverse direction respectively, μ_{LT} is the shear modulus, and ν_{LT} and ν_{TT} are Poisson's ratios.

The transversely isotropic material properties of the local HAp crystal composite are determined by the following rules:

1. The modulus of the longitudinal direction E_L is assumed as 100GPa, and the transverse Poisson's ratio as ν_{TT} =0.2;
2. The other parameters musts follow the relations:

$$\nu_{TT} = \frac{\nu_{TL} + \nu_{LT}}{2} \quad (2.2)$$

$$\frac{\nu_{TL}}{E_T} = \frac{\nu_{LT}}{E_L} \quad (2.3)$$

$$\mu_{LT} = \frac{(E_T + E_L)/2}{2[1 + (\nu_{TL} + \nu_{LT})/2]} \quad (2.4)$$

$$\mu_{TT} = \frac{E_T}{2(1+\nu_{TT})} \quad (2.5)$$

3. Five groups of material constants for the local elements are acquired by choosing values for the moduli ratio, $R = E_T/E_L$, as listed in Table 2.1. The groups of material constants will be assigned to the RUC model to study the effects of variation of local properties on the mechanical response of enamel.

2.4 Orientations

The mechanical properties of a transversely isotropic material is anisotropic, thus orientation should be introduced in order to complete the material property definition. The orientation inside each element varies, so it is necessary to define the orientation for all the elements within the repeating keyhole structure.

Two angles between the symmetric axis of the local longitudinal direction and global coordinate system are required to define the transversely isotropic orientation: the *xz* plane angle θ with respect to the global *x* axis, and the *yz* plane angle ϕ with respect to the global *y* axis. Orientation inside the rod is illustrated in three normal planes in Figure 2.4. The short solid lines represent the longitudinal direction of the HAp-protein composite in the figure. In the inner head region of the model, the angle ϕ=90° and θ=90°. This shows the incorporation of local orientation with the rod direction in the head region. In the tail of the rod, ϕ increases gradually and reaches 180° as it comes to the interrod region. The variation of orientation angles are presented in Figure 2.5. The angles were approximately assigned according to the sketch in Figure 1.5. Detail assignment of the angles for each element is provided in Appendix A.

In the RUC model where the equivalent of two rods is shown, each pair of identical elements shares the same local property definition including orientation.

2.5 Periodic boundary conditions:

Periodic boundary conditions (PBC) must be prescribed on the entire perimeter of the RUC, e.g., top/bottom (or left/right and front/back) surfaces must deform in the same pattern at any instance no matter how the loading conditions are applied. PBC play the most important role in connecting the RUC to the global mechanical behavior. To implement, proper constraints must be imposed on boundaries of corresponding surfaces of the RUC such that it can deform in the periodic pattern so that the deformed RUC can represent the deformed infinite bulk by repeating itself in all three dimensions.

In order to accomplish the PBC, corresponding surfaces need to deform in an identical pattern. The following steps are followed to impose this condition (Figure 2.6):

1. Choose 2 reference nodes (equivalent) A & B;
2. Pick 2 equivalent nodes A1 & B1;
3. Set $\boldsymbol{u}_{A1}-\boldsymbol{u}_{A}=\boldsymbol{u}_{B1}-\boldsymbol{u}_{B}$;
4. Repeat step 2 & 3 for all nodes on equivalent surfaces S_A & S_B;
5. Choose 2 reference nodes (equivalent) C (=A) & D;
6. Pick 2 equivalent nodes C1 & D1;
7. Set $\boldsymbol{u}_{C1}-\boldsymbol{u}_{C}=\boldsymbol{u}_{D1}-\boldsymbol{u}_{D}$;
8. Repeat step 6 & 7 for all nodes on equivalent surfaces S_C & S_D;
9. Choose 2 reference nodes (equivalent) E (=A, C) & F;
10. Pick 2 equivalent nodes E1 & F1;
11. Set $\boldsymbol{u}_{E1}-\boldsymbol{u}_{E}=\boldsymbol{u}_{F1}-\boldsymbol{u}_{F}$;
12. Repeat step 10 & 11 for all nodes on equivalent surfaces S_E & S_F;
13. Remove overlapping equations for corner and edge nodes

This method constrains all of the identical vectors starting from the reference nodes to all other nodes on the surfaces between the two identical surfaces. If all the equivalent vectors are identical, the two surfaces can automatically match each other if the equivalent reference nodes coincide. Figure 2.7 shows the deformed configuration of the PBC-prescribed RUC after a shear loading. From the figure, the unit cells repeat themselves without any gaps or overlaps.

2.6 Global rod properties

In the past, FEM analysis of the effective anisotropic stress-strain relations in enamel were assumed as orthotropic (nine independent constants) (Spears 1997; Shimizu, Macho et al. 2005). However, according to the nature of the microstructure of enamel which consists of repeated rods across the transverse plane, enamel only occupies one plane of symmetry, as shown in Figure 2.8. The macroscopic effective constitutive relation is more appropriately modeled as monoclinic (13 independent constants) as shown in the equation:

$$\begin{pmatrix} \sigma_{11} \\ \sigma_{22} \\ \sigma_{33} \\ \tau_{23} \\ \tau_{31} \\ \tau_{12} \end{pmatrix} = \begin{pmatrix} C_{11} & C_{12} & C_{13} & C_{14} & 0 & 0 \\ C_{12} & C_{22} & C_{23} & C_{24} & 0 & 0 \\ C_{13} & C_{14} & C_{33} & S_{34} & 0 & 0 \\ C_{14} & C_{24} & C_{34} & C_{44} & 0 & 0 \\ 0 & 0 & 0 & 0 & C_{55} & C_{56} \\ 0 & 0 & 0 & 0 & C_{56} & C_{66} \end{pmatrix} \begin{pmatrix} \varepsilon_{11} \\ \varepsilon_{22} \\ \varepsilon_{33} \\ \gamma_{23} \\ \gamma_{31} \\ \gamma_{12} \end{pmatrix} \quad (2.6),$$

where the stiffness tensor $\boldsymbol{C}$ is symmetric ($\boldsymbol{C}=\boldsymbol{C}^T$) and has 13 independent material constants. By determining the values of the 13 constants in the stiffness tensor the effective properties of enamel can be evaluated by the stress-strain relationship for any loading condition.

2.7 Loading conditions

The RUC model is analyzed with six different loading conditions to determine the monoclinic stiffness constants. This is performed with the local properties assigned according to Section 2.4. As shown in Figure 2.9, loadings were executed in six directions on six corner nodes

of the RUC with displacement control, while one corner node is fixed. The loading conditions were chosen in a way so such together with the previously defined PBC, simple uniaxial stress/shear stress fields were able to be generated.

2.8 Stress/Strain field generation

Effective stress fields were able to be generated by dividing the reaction forces of the loading nodes *F* over the surface nominal area *A* where the load was applied, $\sigma = F/A$, as shown in Figure 2.9.

In each of the 6 loading cases, effective strain fields were generated based on the displacements of corner nodes as well as the RUC geometry. As shown in Figure 2.10, displacement vectors of nodes 1, 2 and 3 are monitored with node 0 fixed. The equations employed to calculate strain components are shown below:

$$\varepsilon_x^{ave} = \frac{\Delta u_{1x}}{l}, \quad \varepsilon_y^{ave} = \frac{\Delta u_{2y}}{l}, \quad \varepsilon_z^{ave} = \frac{\Delta u_{3z}}{l} \quad (2.7)$$

$$\varepsilon_{xy}^{ave} = \frac{1}{2l}\left(\Delta u_{2x} + \Delta u_{1y}\right), \quad \varepsilon_{yz}^{ave} = \frac{1}{2l}\left(\Delta u_{3y} + \Delta u_{2z}\right), \quad \varepsilon_{zx}^{ave} = \frac{1}{2l}\left(\Delta u_{1z} + \Delta u_{3x}\right) \quad (2.8)$$

The equations above for computing effective strain fields are independent of loading conditions therefore were applied on all loading cases.

The stress field and strain field calculated based on the deformed shapes of the RUC model are presented in Table 2.2 and Table 2.3 for the case where local element properties are assigned with *R*=0.2, in which $\boldsymbol{\sigma}^{i}/\boldsymbol{\varepsilon}^{i}$ are the stress/strain vector of the *ith* loading case, followed by the notation of specific loading conditions. The stress field is presented by the unit of GPa while the strain field is unitless. For the other cases with different *R* values as local properties input, the same displacement control loading conditions were applied and the same equations were used for calculation of stress/strain fields.

2.9 Stiffness tensor

In order to find the macroscopic mechanical behavior of enamel, 13 independent equations were needed to solve for the 13 constants in the monoclinic stiffness tensor of enamel.

In each loading case for the corresponding strain and stress vectors, $\boldsymbol{\varepsilon}^{\boldsymbol{i}}$ and $\boldsymbol{\sigma}^{\boldsymbol{i}}$, one can extract 6 equations. Suppose the total number of loading cases is i, then there are $6\times i$ equations in all. It's common that some of the equations were not linearly independent. In order to calculate all 13 constants, enough loading cases should be executed and the loading conditions should be chosen in a way that all the constants contribute in the equation. In this work, 6 loading cases were applied. This might lead to overconstraints since there are more than 13 equations. To overcome the overconstraints, and also to impose absolute symmetry on the stiffness tensor, rearrangement of the equations and the singular value decomposition method (SVD) are employed.

The equation $\boldsymbol{\sigma}^{i}=\boldsymbol{C}\,\boldsymbol{\varepsilon}^{i}$ for the i^{th} loading case can be rearranged in the form $\boldsymbol{\sigma}^{i}=\boldsymbol{E}^{i}\boldsymbol{C}^{*}$ where

$$E^{i}=\begin{bmatrix} \varepsilon_{11}^{i} & \varepsilon_{22}^{i} & \varepsilon_{33}^{i} & \gamma_{23}^{i} & 0 & 0 & 0 & 0 & 0 & 0 & 0 & 0 & 0 \\ 0 & \varepsilon_{11}^{i} & 0 & 0 & \varepsilon_{22}^{i} & \varepsilon_{33}^{i} & \gamma_{23}^{i} & 0 & 0 & 0 & 0 & 0 & 0 \\ 0 & 0 & \varepsilon_{11}^{i} & 0 & 0 & \varepsilon_{22}^{i} & 0 & \varepsilon_{33}^{i} & \gamma_{23}^{i} & 0 & 0 & 0 & 0 \\ 0 & 0 & 0 & \varepsilon_{11}^{i} & 0 & 0 & \varepsilon_{22}^{i} & 0 & \varepsilon_{33}^{i} & \gamma_{23}^{i} & 0 & 0 & 0 \\ 0 & 0 & 0 & 0 & 0 & 0 & 0 & 0 & 0 & 0 & \gamma_{13}^{i} & \gamma_{12}^{i} & 0 \\ 0 & 0 & 0 & 0 & 0 & 0 & 0 & 0 & 0 & 0 & 0 & \gamma_{13}^{i} & \gamma_{12}^{i} \end{bmatrix} \quad (2.9),$$

$$C^{*}=\begin{bmatrix} C_{11} & C_{12} & C_{13} & C_{14} & C_{22} & C_{23} & C_{24} & C_{33} & C_{34} & C_{44} & C_{55} & C_{56} & C_{66} \end{bmatrix}^{T} \quad (2.10).$$

By combining 6 loading cases, the equation becomes $\boldsymbol{A}=\boldsymbol{B}\boldsymbol{C}^{*}$ where $\boldsymbol{A}_{36x1}=[\,\boldsymbol{\sigma}^{1T},\ldots\,\boldsymbol{\sigma}^{6T}]^{\mathrm{T}}$, $\boldsymbol{B}_{36x13}=[\,\boldsymbol{E}^{1T},\ldots\,\boldsymbol{E}^{6T}]^{\mathrm{T}}$.

Since $\boldsymbol{B}$ is a non-square matrix, the SVD method (Mottershead and Foster 1991; Ramanujam and Nakamura 2007) is necessary to solve the transformed stiffness tensor. It is an effective technique to solve or get best estimation of linear least-square problems when matrices

that are singular or non-squared are involved. When the matrix, for instance, $\boldsymbol{B}$, is not square, it can be decomposed as $\boldsymbol{B}=\boldsymbol{USV}^{\boldsymbol{T}}$, where $\boldsymbol{U}$ is a column-orthogonal matrix, $\boldsymbol{S}$ is a square diagonal matrix, and $\boldsymbol{V}$ is a square orthogonal matrix. Once $\boldsymbol{B}$ is decomposed, the generalized inverse form of $\boldsymbol{B}$ can be expressed as $\boldsymbol{VS}^{-1}\boldsymbol{U}^{\boldsymbol{T}}$, so $\boldsymbol{C}$ can be calculated by $\boldsymbol{C}=\boldsymbol{VS}^{-1}\boldsymbol{U}^{\boldsymbol{T}}\boldsymbol{A}$. Detail information about the decomposition of matrix $\boldsymbol{B}$ is provided in Appendix B.

2.10 Summary

A periodic representative unit cell with 240 brick elements was established to represent the microstructure of the human tooth enamel. Five groups of locally transversely isotropic properties and appropriate orientations were assigned to each element in the model. A special periodic boundary condition was prescribed on the boundary of the unit cell model.

Six loading conditions were applied on the unit cell model for each model with various local properties. The stress and strain fields were generated according to the reaction forces and the nodal displacements.

The effective mechanical properties of the enamel bulk will be presented in the next chapter according to the loading cases on the unit cell model. The effects of local properties variations on the effective mechanical properties will be studied as well as the microstructure effects.

R	E_L (GPa)	E_T (GPa)	v_{LT}	v_{TT}	μ_{LT} (GPa)
1	100	100	0.2	0.2	41.67
0.5	100	50	0.27	0.2	31.25
0.2	100	20	0.33	0.2	25
0.1	100	10	0.36	0.2	22.92
0.05	100	5	0.38	0.2	21.88

Table 2.1 Local properties of elements with ratios of $R = E_T/E_L$

	$\boldsymbol{\sigma}^1$x tension	$\boldsymbol{\sigma}^2$y tension	$\boldsymbol{\sigma}^3$z tension	$\boldsymbol{\sigma}^4$yz shear	$\boldsymbol{\sigma}^5$xz shear	$\boldsymbol{\sigma}^6$xy shear
σ_{xx}	25.61	0	0	0	16.81	14.74
σ_{yy}	0	34.16	0	16.84	0	14.74
σ_{zz}	0	0	50.27	16.84	16.81	0
τ_{yz}	0	0	0	16.84	0	0
τ_{zx}	0	0	0	0	-16.81	0
τ_{xy}	0	0	0	0	0	-14.74

Table 2.2 Effective stress fields under 6 loading cases with local property ratio R=0.2

	$\boldsymbol{\varepsilon}^1$x tension	$\boldsymbol{\varepsilon}^2$y tension	$\boldsymbol{\varepsilon}^3$z tension	$\boldsymbol{\varepsilon}^4$yz shear	$\boldsymbol{\varepsilon}^5$xz shear	$\boldsymbol{\varepsilon}^6$xy shear
ε_{xx}	1	-0.14	-0.14	-0.16	0.61	0.51
ε_{yy}	-0.11	1	-0.12	0.54	-0.11	0.37
ε_{zz}	-0.07	-0.08	1	0.38	0.29	-0.07
γ_{yz}	-0.06	0.18	0.27	1.07	0.05	0.04
γ_{zx}	0	0	0	0	-1.10	-0.13
γ_{xy}	0	0	0	0	-0.15	-1.11

Table 2.3 Effective strain fields under 6 loading cases with local property ratio R=0.2

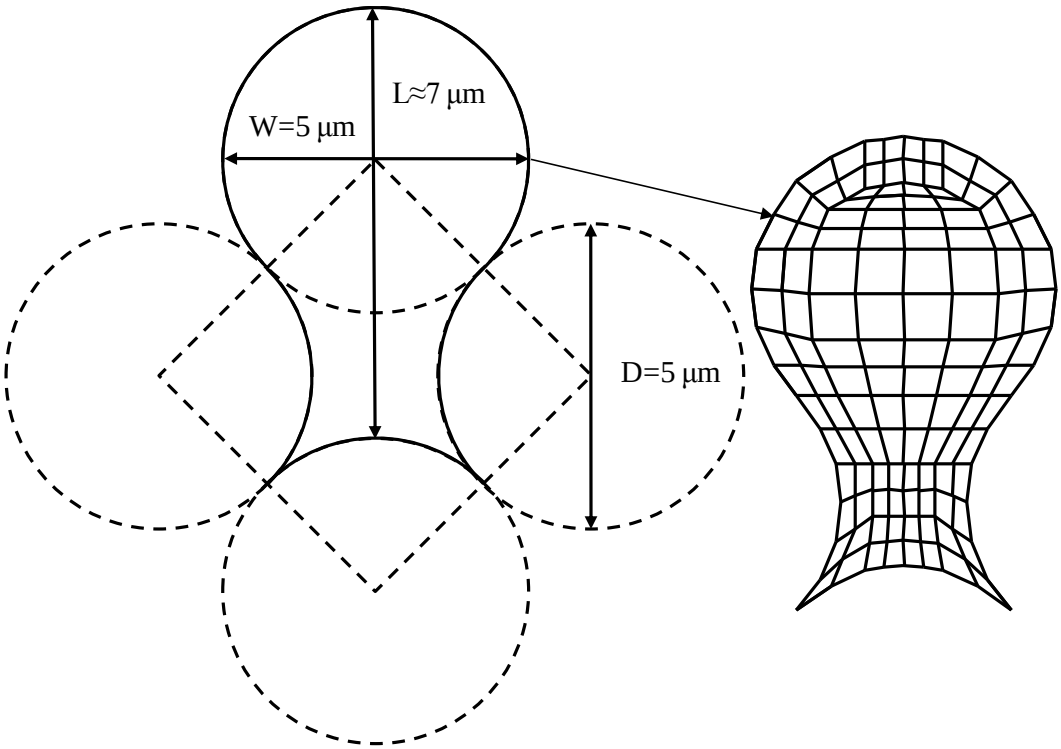

Figure 2.1 Illustration of the keyhole-shaped rod and interrod region contour and the mesh development (right)

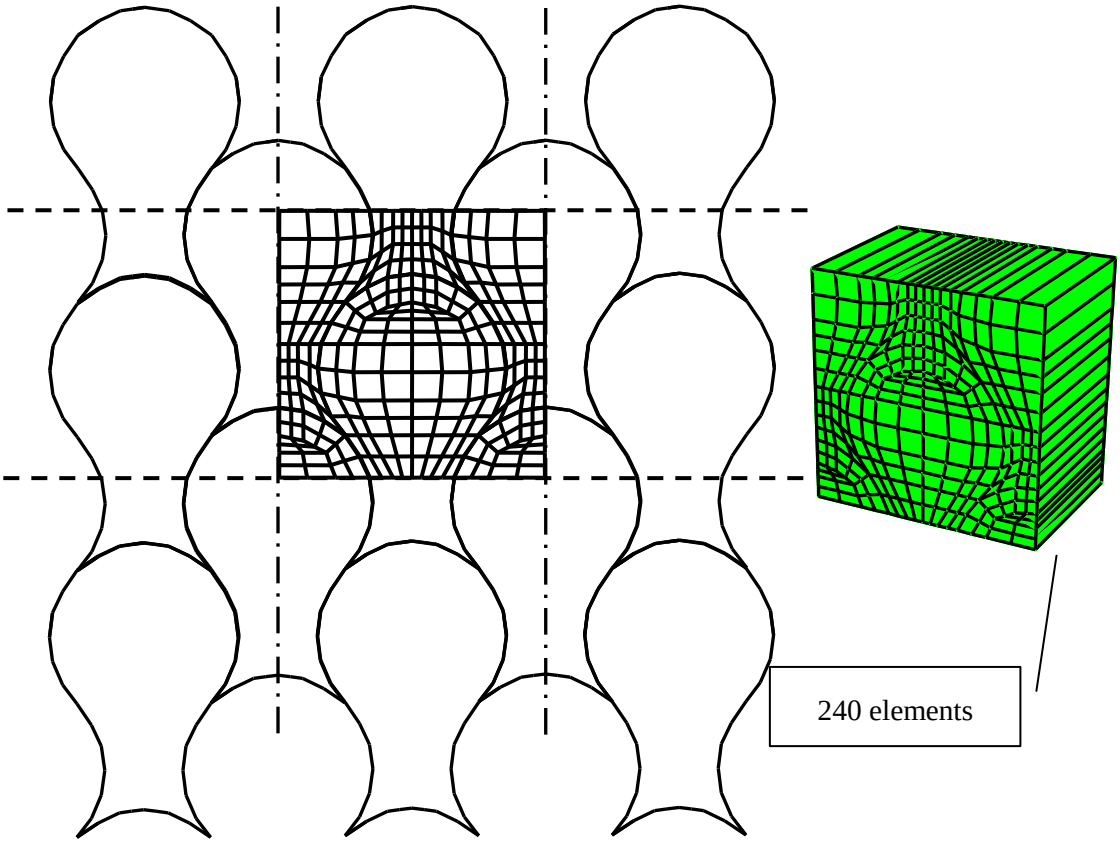

Figure 2.2 The representative unit cell (RUC) of the enamel bulk model shown surrounded by the enamel rods (left), and the 3D extruded finite element mesh (right)

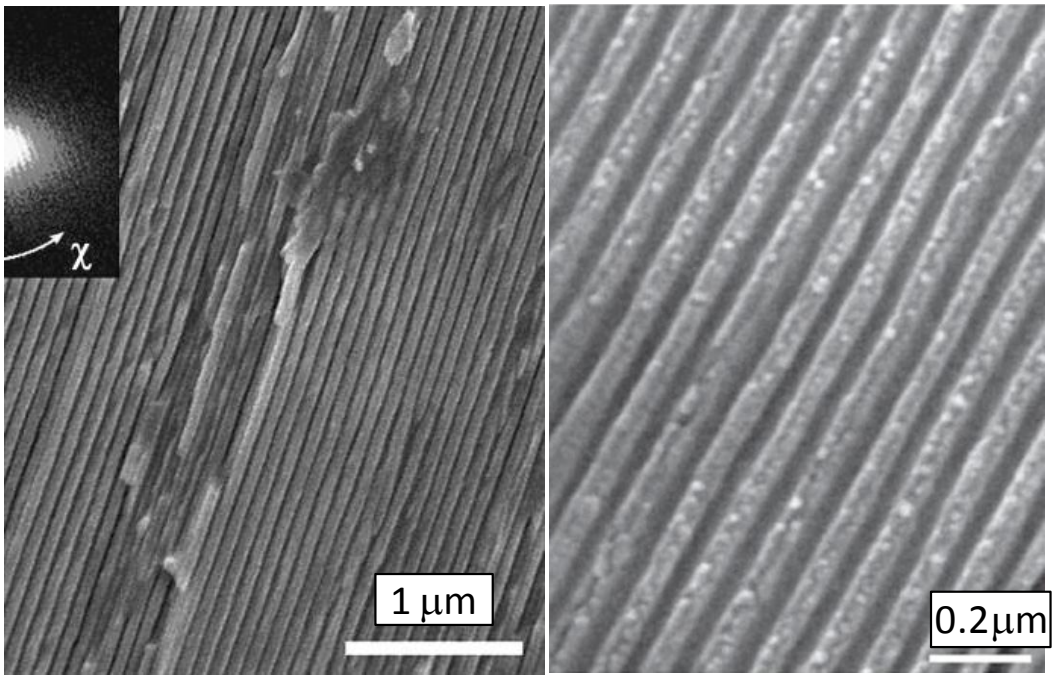

Figure 2.3 SEM images of localized HAp-protein composites within an enamel rod (Jiang, Liu et al. 2005)

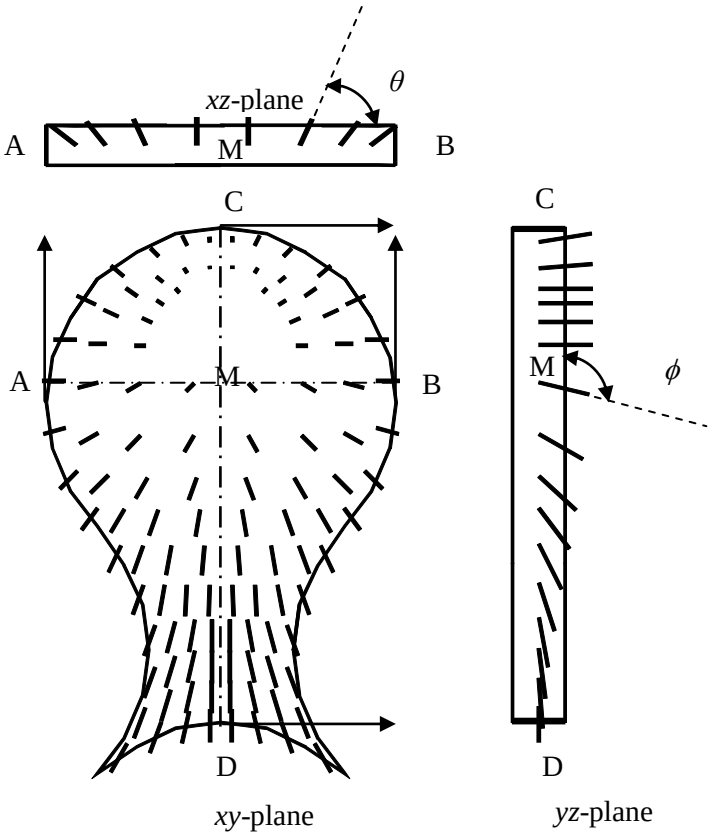

Figure 2.4 Orientation of HAp-protein composites inside the enamel rod shown in three normal cut views. Orientation is described by the two angles presented in the figure.

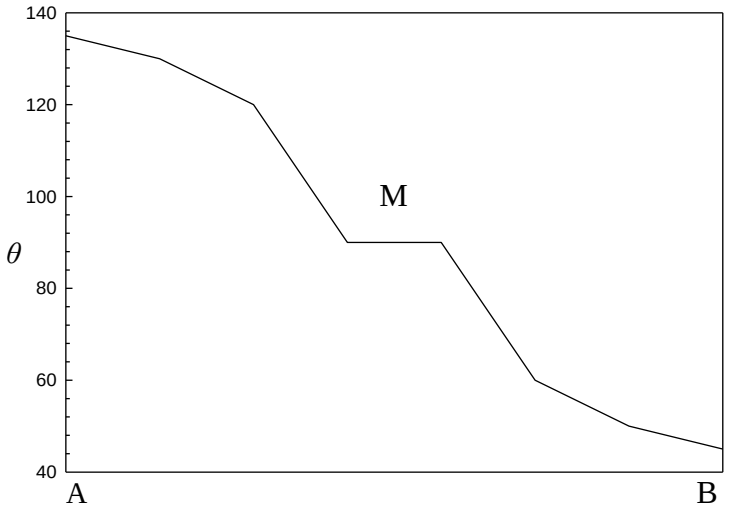

(a) *xz*-plane

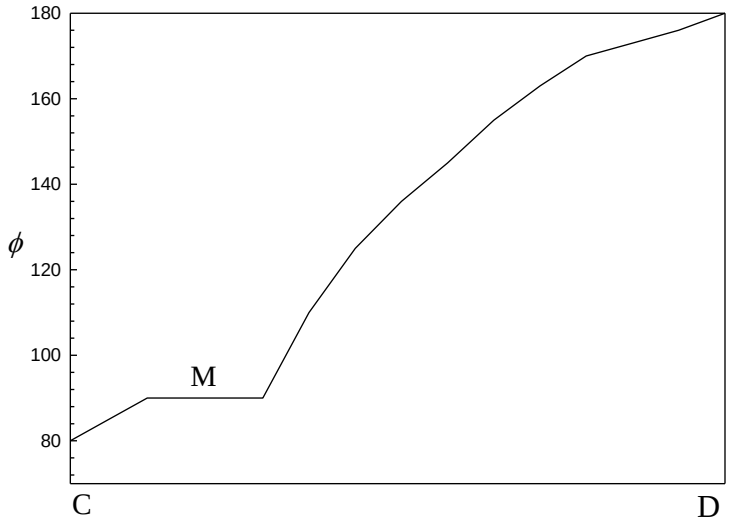

(b) *yz*-plane

Figure 2.5 HAp crystal orientation with respect to relative position within an enamel rod, (a) Horizontal cut view through head; (b) vertical cut view through the symmetry line. Spatial positions coincide with Figure 2.4

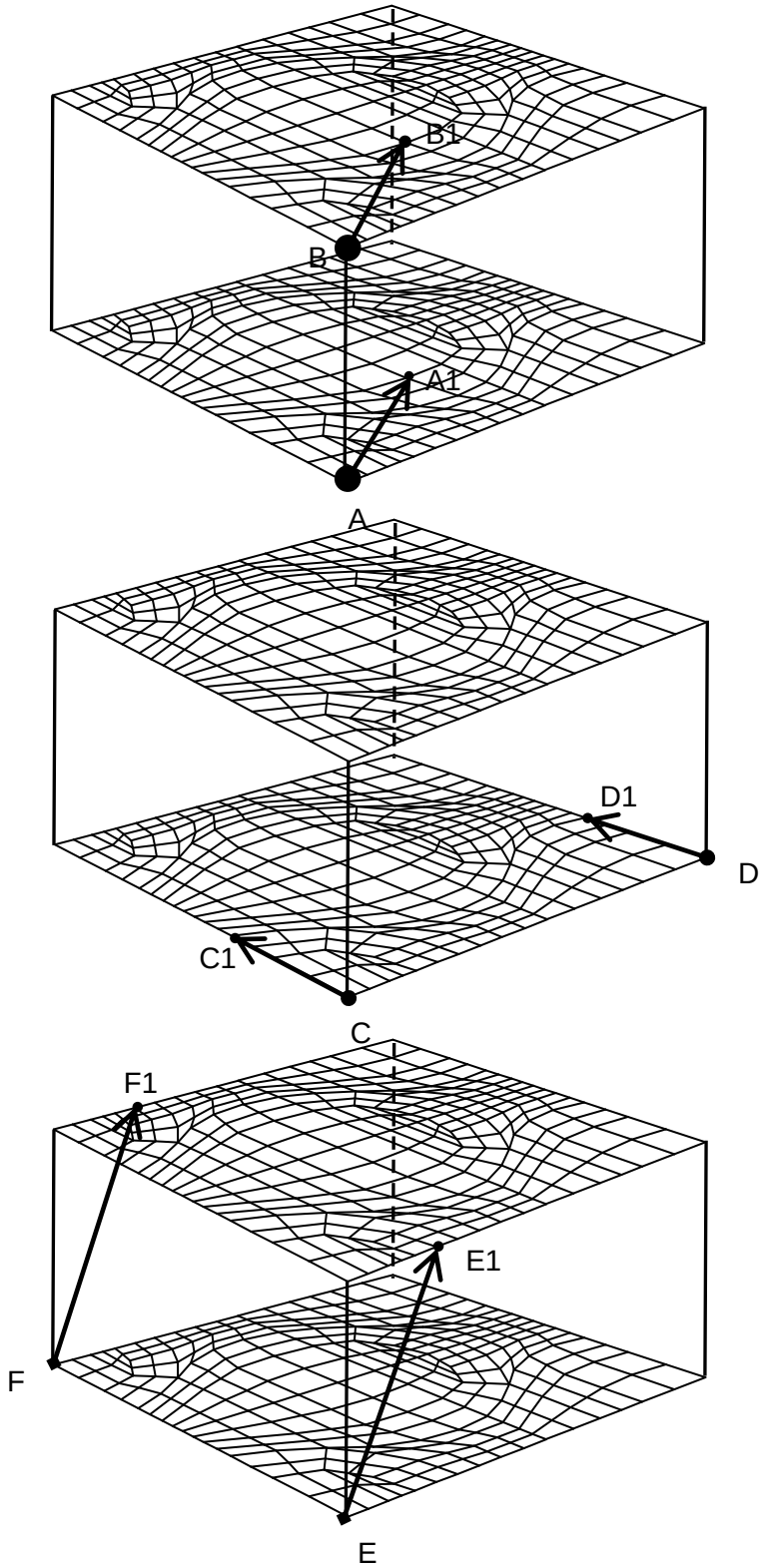

Figure 2.6 Method of prescribing periodic boundary conditions (PBC) to the representative unit cell

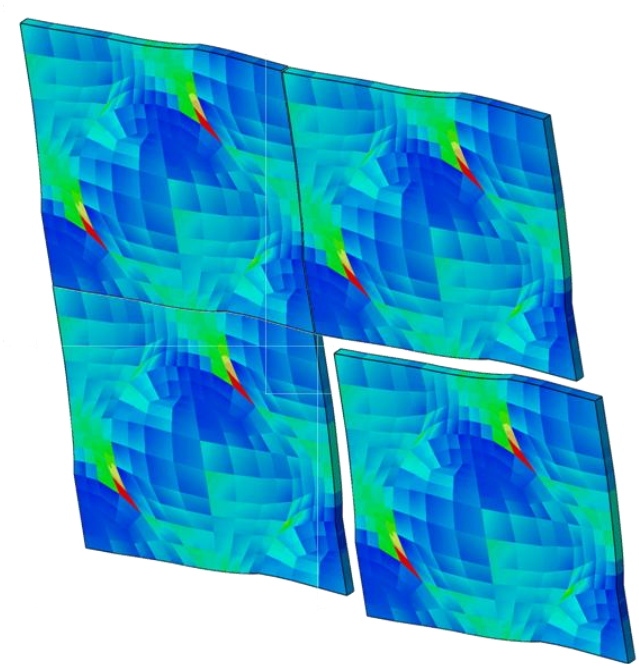

Figure 2.7 Reassembly of deformed RUC with PBC applied on the boundaries, showing the matching of boundary deformations.

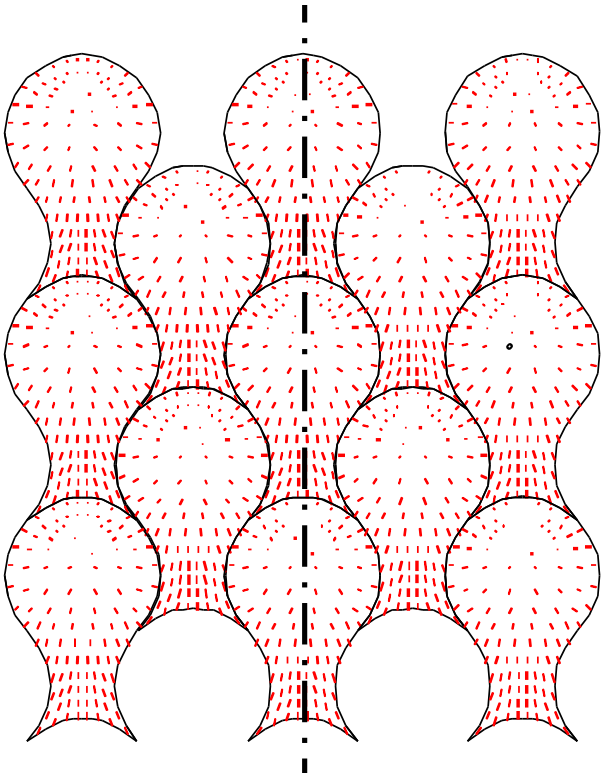

Figure 2.8 Global enamel rod assembly with localized material orientation. The structure only occupies one symmetric plane shown by a dashed line, represented by a monoclinic stiffness tensor.

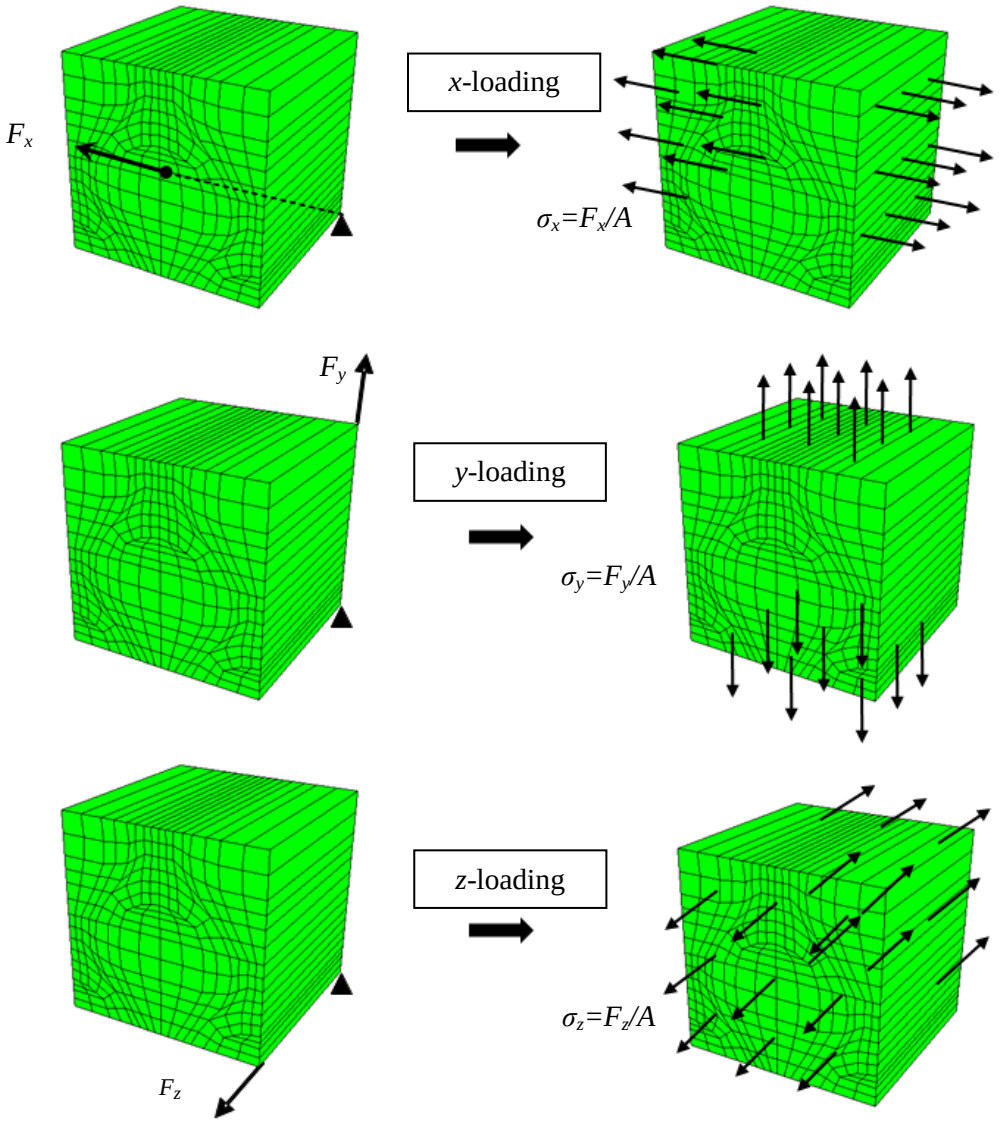

Figure 2.9 The six loading conditions on the representative unit cell model, showing the applied load and boundary condition and the resulting stress direction.

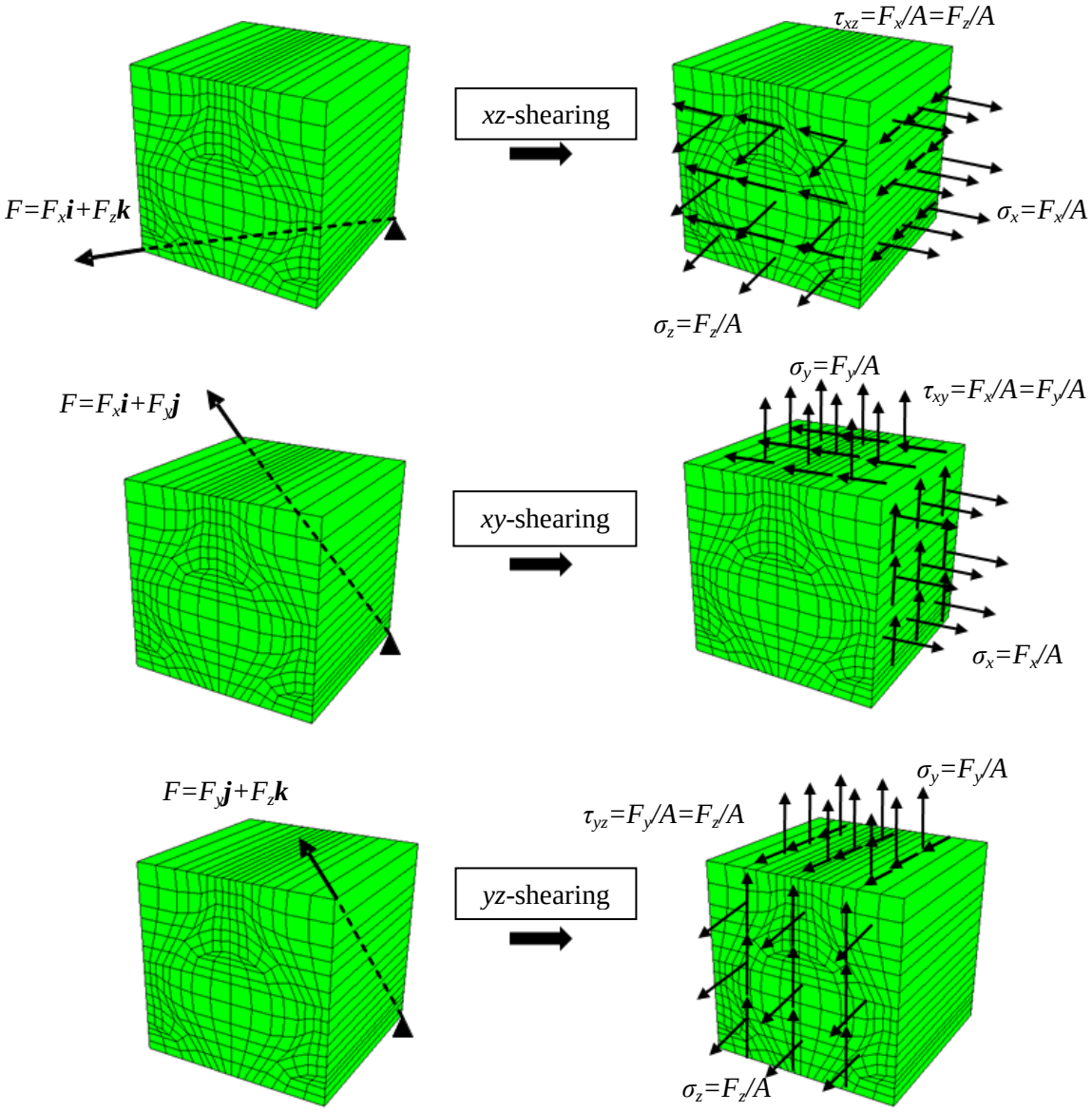

Figure 2.9 The six loading conditions on the representative unit cell model, showing the applied load and boundary condition and the resulting stress direction. (continued)

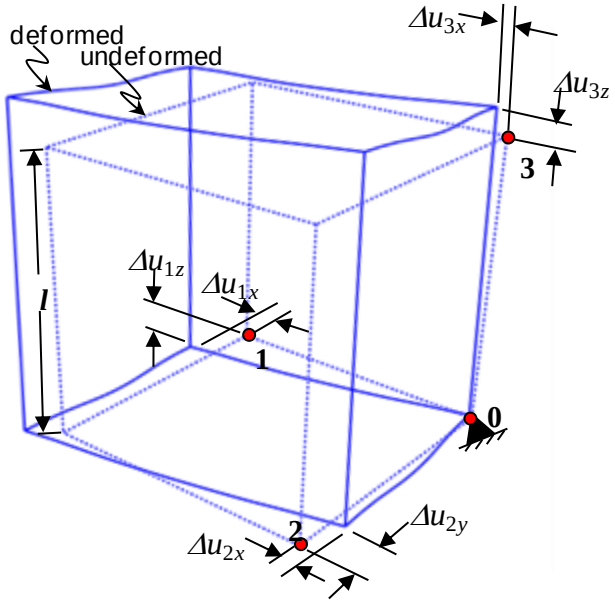

Figure 2.10 Strain field generation method on the deformed RUC model

Chapter 3 Results and discussion

The effective mechanical properties of the enamel bulk determined from the six loading cases on the unit cell model are presented, and the effective moduli are compared with experimental microindentation data. Simulation of a spherical indentation is performed, where the effects of microstructure and the local property variations on the effective mechanical properties are studied.

3.1 Stress concentrations

Mises stress (a scalar stress value that is computed from the stress tensor or the principal stresses), first principal stress and pressure stress contours under six different loading conditions with local property ratio of E_T/E_L=0.2 are presented in Figure 3.1, Figure 3.2and Figure 3.3. Stress concentrations are observed on the boundary of adjacent enamel rods. This indicates the enamel rod boundary is the most likely spot where micro fracture and erosion would occur under critical or repeated loading due to locally high strains which will disrupt the HAp crystal-protein composite.

3.2 Effective stiffness tensor

The effective stiffness tensor was calculated by generating the effective stress and strain fields of the representative unit cell under six loading cases and applying the singular value decomposition method.

Effects of variation in local properties on the effective stiffness tensor were investigated. Five different ratios of E_T/E_L were chosen to vary the local (element-scale) material properties of the unit cell model. The variations in E_T/E_L were achieved by changing E_T while E_L is fixed as 100 GPa. Table 3.1 shows the calculated effective stiffness tensors with different ratios of E_T/E_L.

Changes of diagonal components in the stiffness tensor with the variation of E_T/E_L are plotted in Figure 3.4. Larger effects of E_T variations on normal stress-strain constants C_{11}, C_{22} and C_{33} were observed. Variation of E_T/E_L when E_T is lower causes greater reduction in C_{11} and C_{22} components. C_{11} and C_{22} are more sensitive to E_T changes than C_{33}. The other components of the stiffness tensor have mixed behaviors on variation of E_T/E_L as seen in Figure 3.5.

3.2.1 Effectiveness of homogeneity

An effective homogeneous monoclinic model with the identical mesh of the RUC model was built with the material properties assigned as the calculated effective stiffness tensor for every E_T/E_L ratio to examine the effectiveness of the homogeneity. For each E_T/E_L ratio, the effective homogeneous monoclinic model was loaded in the same loading condition as the original model and analyzed for its resultant strain and stress fields where were compared with the original heterogeneous model. The difference is less than 0.0001% for all of the components in both strain and stress fields for every E_T/E_L ratio. The homogeneous model behaves effectively identical to the heterogeneous model in terms of the strain and stress fields.

3.3 Effective Young's modulus

Changes in effective young's modulus in normal directions verses variation of E_T/E_L are plotted in Figure 3.6. $E_z>E_y>E_x$ always. This shows the evidence for the statement that the stiffest direction of the enamel is the longitudinal direction in which the rods run. E_x and E_y decrease faster than E_z as E_T decreases. Thus, changes in the local transverse modulus have less effect on the global longitudinal effective modulus than on the transverse ones.

The constant relation of the effective moduli from the model, $E_y>E_x$, shows that the in plane modulus (*xy* plane perpendicular to the rod axes) is highest in the *y* direction which is along the keyhole shaped head-tail direction, and least orthogonal to this direction. This has

implications to understanding the structure of the enamel rods in the tooth crown, where the rod heads point in the direction of the tooth cusp around the entire circumference of the tooth. The data indicates that the higher stiffness in the direction of the head-tail may allow enamel to absorb compressive stresses that are generated due to occlusal contact conditions (such as mastication with the primary molars).

Normalized E_x and E_y over E_z are plotted in Figure 3.7. Compared to E_y, E_x decreases faster as E_T decreases. This leads to the conclusion that the softest direction is perpendicular to the symmetric plane of the enamel. As E_T/E_L decreases from 1 (locally isotropic) to 0.05 (E_L 20 times larger than E_T), E_x/E_z and E_y/E_z drop from 1 (globally isotropic) to 0.2 and 0.35 respectively. The high local anisotropy leads to high global anisotropy.

Experimental measurement of a spherical microindentation on the occlusal and transverse surfaces of an enamel sample with a radius of 200 μm was conducted. The effective moduli were calculated by applying Oliver and Pharr method (Oliver and Pharr 1992) to interpret the unloading curves. The modulus of the occlusal surface was measured as E_{norm}=56.5 ±2.27 GPa and the modulus of the transverse surface was measured as E_{tran}=34.5 ±3.84 GPa. The ratio of E_{tran}/E_{norm} is 0.61, and ranges from 0.52 to 0.71 when the standard derivations are considered. Similar ratios were found by He et al. (He, Fujisawa et al. 2006), where for shallower indentations (contact radius of ~3 μm) a ratio of E_{tran}/E_{norm} = 0.57 was observed from the data. Due to the difficulty of identifying polished sample surface angle, it is difficult to determine the direction the 'transverse' modulus E_{tran} was measured, but the value of E_{tran} should lie between E_x and E_y since the transverse modulus was measured in the xy plane. The ratio of E_{tran}/E_{norm} matches the ratios of E_x/E_z and E_y/E_z well when the local properties ratio E_T/E_L ranges from 0.1 to 0.45.

Measurement on the local elastic moduli of an enamel sample using Atomic Force Acoustic Microscopy shows approximately 40-50% difference between the moduli of local properties which approximately correspond to the local property E_T and E_L in the model (Zhao, Cao et al. 2010). The ratio of E_T/E_L from the AFAM measurement has good agreement with the 0.1-0.45 range of suitable ratio of E_T/E_L where the microindentation data agrees with the model effective modulus ratio.

3.4 Effects of model geometry

Effects of variation of the representative unit cell model geometry on the effective stiffness tensor were studied. The model was elongated in the *y* direction by the factor of 1.5 from the original size. The calculated effective stiffness tensors of the alternative model and the original model were compared in Figure 3.8. The constant C_{22} has an increase of approximately 6%. The changes in other constants are not as large as C_{22}.

The geometry variation of the model has limited effects on the effective stiffness tensor of the model.

3.5 Instrumented indentation

3.5.1 Stress contours of indented samples

Mises stress contours for the model with local property ratio of 0.2 are shown in 3 steps until the full penetration depth in Figure 3.9. The stresses concentrated on the head region of the enamel rods and were transferred in the longitudinal direction where more resilient dentin lies. The orientation of HAp-protein composites was more perpendicular to the occlusal surface in the rod head region, providing their highest stiffness in this direction.

3.5.2 Size variation

Depth controlled spherical indentation with depth of Δ=1 μm was conducted with 3 bulk models on the occlusal surfaces with different number of unit cells (3×6×10, 6×12×15, 6×12×22 with dimensions of 21×42×10.15 μm, 42×84×29.75 μm, 42×84×168.00 μm) to determine the necessary model size to eliminate boundary effects. The loading curves are plotted in Figure 3.10.

In the initial loading stage, the difference of loading forces was not significant with varied thickness. As the penetration went deeper, the difference in loading forces became larger gradually. Also, with the increase of model size, the final indentation load decreases approximately 80%.

The large difference shows the important effect of sample size on the results of the indentation loading curve. If the sample is not large enough, the stress propagates towards the bottom as the penetration is in progress. At certain penetrating height, the stress reaches the relatively rigid surface on which the sample is placed. Thus a 'substrate effect' takes place and the rigidity of the substrate increases the loading force considerably. The substrate effect is avoidable by increasing the sample size with respect to the indentation depth. From the stress contour of the sample bottom at the full loading point, the stress is not significant with the thickness layer of 22. The sample thickness is enough to avoid the substrate effect. The indentation depth is ~0.6% of the model thickness.

The effect of the side constraints on the result accuracy is investigated using the 6×12×22 model where the circumferential surfaces are fixed. The loading curves for the constrained and unconstrained models are plotted in Figure 3.11. The constrained model has a large load resistance than the unconstrained model. In a realistic test, the loading curve should lie in

between the two curves shown in Figure 3.11 since the true boundary condition of the sides is in between free ends and totally fixed.

3.5.3 Local property ratio variation

Depth controlled spherical indentation with Δ=1 μm was conducted using 3 bulk models on the occlusal surfaces with different local property ratios (E_T/E_L=0.1, 0.2 and 0.5). A fixed model size of 6×12×22 was used. The loading curves are plotted in Figure 3.12.

The difference in the loading forces is small for the initial penetration, and becomes larger as Δ increases. At the full depth of indentation, the difference in loading forces is 30% between E_T/E_L=0.2 and 0.5 and is 50% between E_T/E_L=0.1 and 0.5. As E_T increases while E_L is fixed, the sample is more resistant to indentation.

3.5.4 Comparison of heterogeneous/homogeneous models

An effective homogeneous monoclinic bulk model, the same size of the heterogeneous bulk model, was established using the 13 effective monoclinic property constants listed in Table 3.1. The model was constructed for local property ratios of E_T/E_L=0.1 and 0.2 to compare the mechanical behaviors of heterogeneous and corresponding homogeneous models under spherical micro-indentation.

The same depth controlled spherical indentation with Δ=1 μm was conducted on the homogeneous models and the loading curves were plotted together with the heterogeneous models in Figure 3.13. From the plots, the loading curves of the effective homogeneous models behave similarly to the heterogeneous models, with slightly smaller loading forces over the entire indentation depth range.

The difference between loading forces are plotted as a percentage with respect to penetration depth for each pair of the heterogeneous/homogeneous models in Figure 3.14. The

values were calculated by dividing the force difference over the force of the heterogeneous model at each penetration depth: $\Delta F=(F_{heter}-F_{homo})/F_{heter} \times 100\%$.

As seen in the plot, ΔF was as large as 15% and 10% for E_T/E_L=0.1 and 0.2 respectively in the initial contact period and dropped rapidly to close to 1% as the penetration depth Δ reached approximately 60nm. After the critical depth, ΔF remained almost constant as 1-2%.

The effect of the specific enamel microstructure of the heterogeneous models accounts for the large difference between the heterogeneous and homogeneous models for Δ < 60nm. With Δ=60 nm, the theoretical contact radius is $a \approx 5$ μm for a rigid spherical indenter with radius R=200 μm. Considering the size of one enamel rod is about 5×7 μm, the indenter is only in contact with a fraction of the enamel rod at the initial loading step and gradually the contact area increases to the entire enamel rod and possibly covers around 4 rods when Δ reaches 60 nm where the effects of the localized microstructure decrease for the larger contact area. The microstructure size effects ends after Δ>60 nm, at which point homogenization becomes effective.

Closer inspection of Figure 3.14 also shows undulations in the value of ΔF as a function of indentation depth beyond the critical depth. Peaks in ΔF are observed at 200nm and ~640nm, with the 200 nm peak more pronounced and the 640 nm peak broader. The contact radii at the two peaks are ~9 μm and 15 μm, respectively. These contact radii coincide with the periodicity in the enamel microstructure which repeats every ~5 microns. The peak at 640 nm is less pronounced due to the fact that the contact circumference is distributed over more enamel rods for the larger radius, which averages out the microstructural effect and mitigates the differences. Thus the enamel microstructure is captured in the differences between the homogeneous and heterogeneous model at three discrete length scales corresponding to the repeating rods.

ΔF is consistently smaller for the model with E_T/E_L=0.2 compared to that with E_T/E_L=0.1. This indicates the anisotropic local properties, which are regulated by the microstructure, affect the indentation loading behavior at the modeled indentation depths.

3.5.5 Stress contours of homogeneous samples

From Figure 3.15, the difference is presented for the stress distribution of heterogeneous model and effective homogeneous model at full penetration. In the homogeneous model, the stresses are sustained beneath the contact area rather than transferred deeper into the sample, as in the heterogeneous model. The maximum Mises stress occurred at a depth of 8.47 μm beneath the surface for the heterogeneous model. The corresponding depth of maximum Mises stress was 4.97 μm for the homogeneous model. Although the loading curves were similar, the stress distribution configurations of the original (heterogeneous) model and the effective (homogeneous) model are considerably different. From Figure 3.15, the contact stress distribution has discrete stress concentrations on the surface for the heterogeneous model which correspond to the enamel rod heads. Due to the distribution of the contact pressure over many enamel rods, the maximum contact pressure for the heterogeneous model was lower than the homogeneous model (0.96 GPa compared with 1.05 GPa). This indicates that the homogenization cannot illustrate the microstructure effects of the heterogeneous model.

E_T/E_L	C_{11}	C_{12}	C_{13}	C_{14}	0	0
	C_{12}	C_{22}	C_{23}	C_{24}	0	0
	C_{13}	C_{23}	C_{33}	C_{34}	0	0
	C_{14}	C_{24}	C_{34}	C_{44}	0	0
	0	0	0	0	C_{55}	C_{56}
	0	0	0	0	C_{56}	C_{66}
1	111.11	27.78	27.78	0	0	0
	27.78	111.11	27.78	0	0	0
	27.78	27.78	111.11	0	0	0
	0	0	0	41.67	0	0
	0	0	0	0	41.67	0
	0	0	0	0	0	41.67
0.5	60.23	14.42	15.00	-0.43	0	0
	14.42	70.02	16.39	-3.63	0	0
	15.00	16.39	78.76	-4.08	0	0
	-0.43	-3.63	-4.08	29.19	0	0
	0	0	0	0	26.55	-1.50
	0	0	0	0	-1.50	25.28
0.2	26.35	4.05	3.99	0.41	0	0
	4.05	35.96	5.85	-4.06	0	0
	3.99	5.85	53.02	-5.72	0	0
	0.41	-4.06	-5.72	19.90	0	0
	0	0	0	0	15.52	-1.86
	0	0	0	0	-1.86	13.40
0.1	14.41	0.99	0.26	0.93	0	0
	0.99	21.65	2.21	-3.38	0	0
	0.26	2.21	42.11	-5.82	0	0
	0.93	-3.38	-5.82	15.45	0	0
	0	0	0	0	10.76	-1.55
	0	0	0	0	-1.55	8.47
0.05	8.01	-0.14	-1.28	1.14	0	0
	-0.14	12.99	0.66	-2.65	0	0
	-1.28	0.66	34.95	-5.47	0	0
	1.14	-2.65	-5.47	12.07	0	0
	0	0	0	0	7.66	-1.13
	0	0	0	0	-1.13	5.32

Table 3.1 Effective stiffness tensors (×GPa) with variation of E_T/E_L

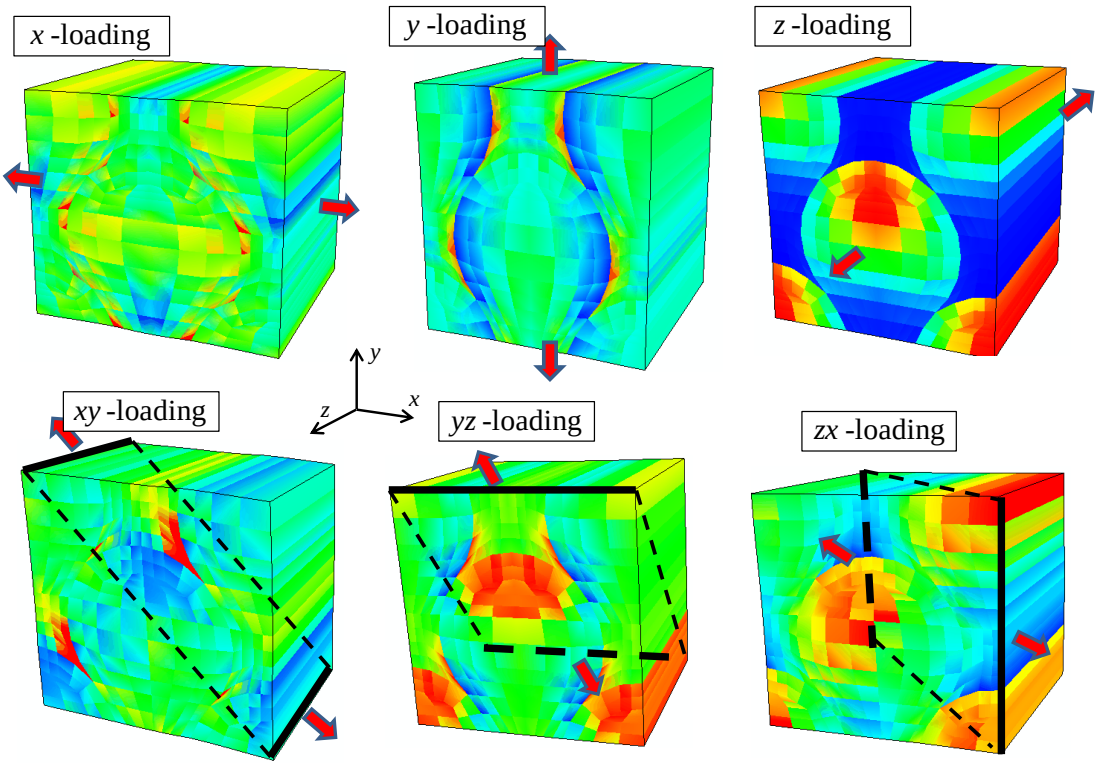

Figure 3.1 Resultant Mises stress contours of the unit cell under 6 loading conditions (E_T/E_L=0.2)

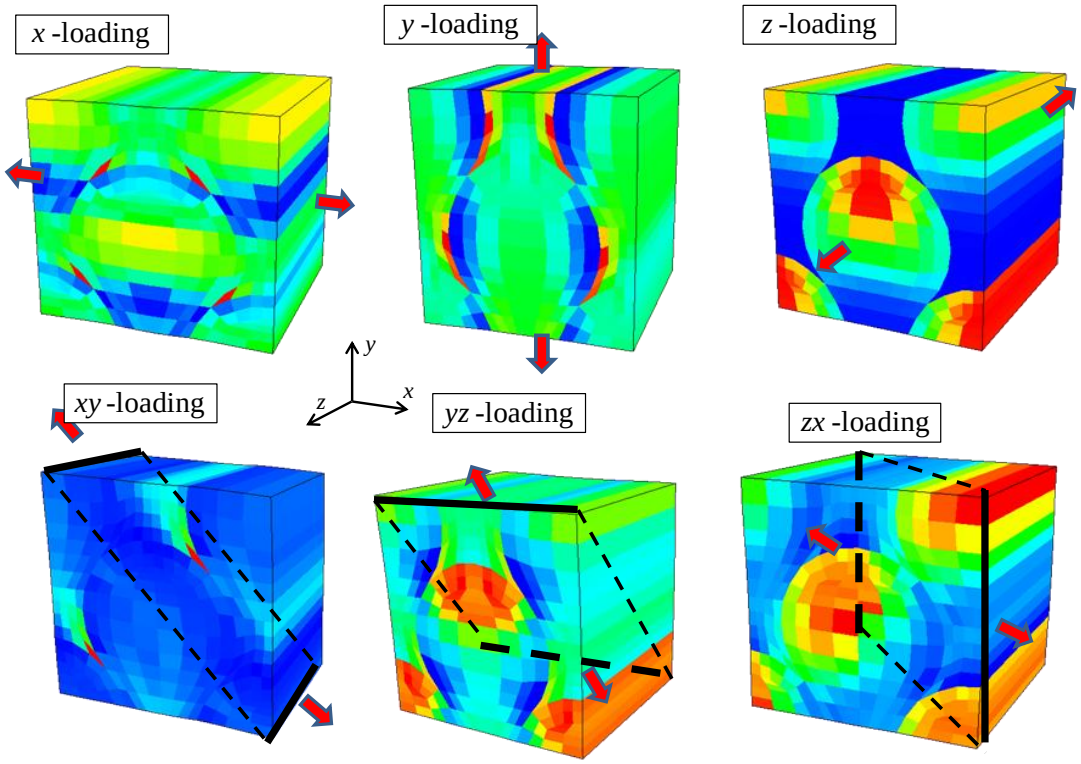

Figure 3.2 First principal stress contours of the unit cell under 6 loading conditions (E_T/E_L=0.2)

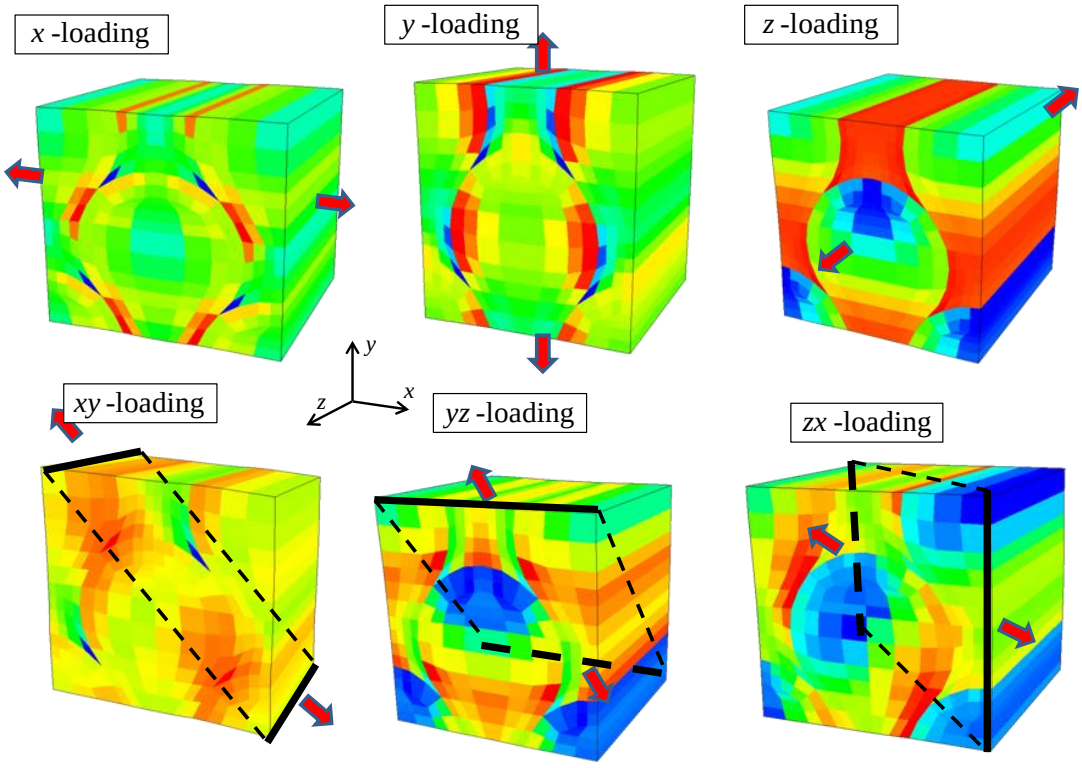

Figure 3.3 Resultant pressure stress contours of the unit cell under 6 loading conditions (E_T/E_L=0.2)

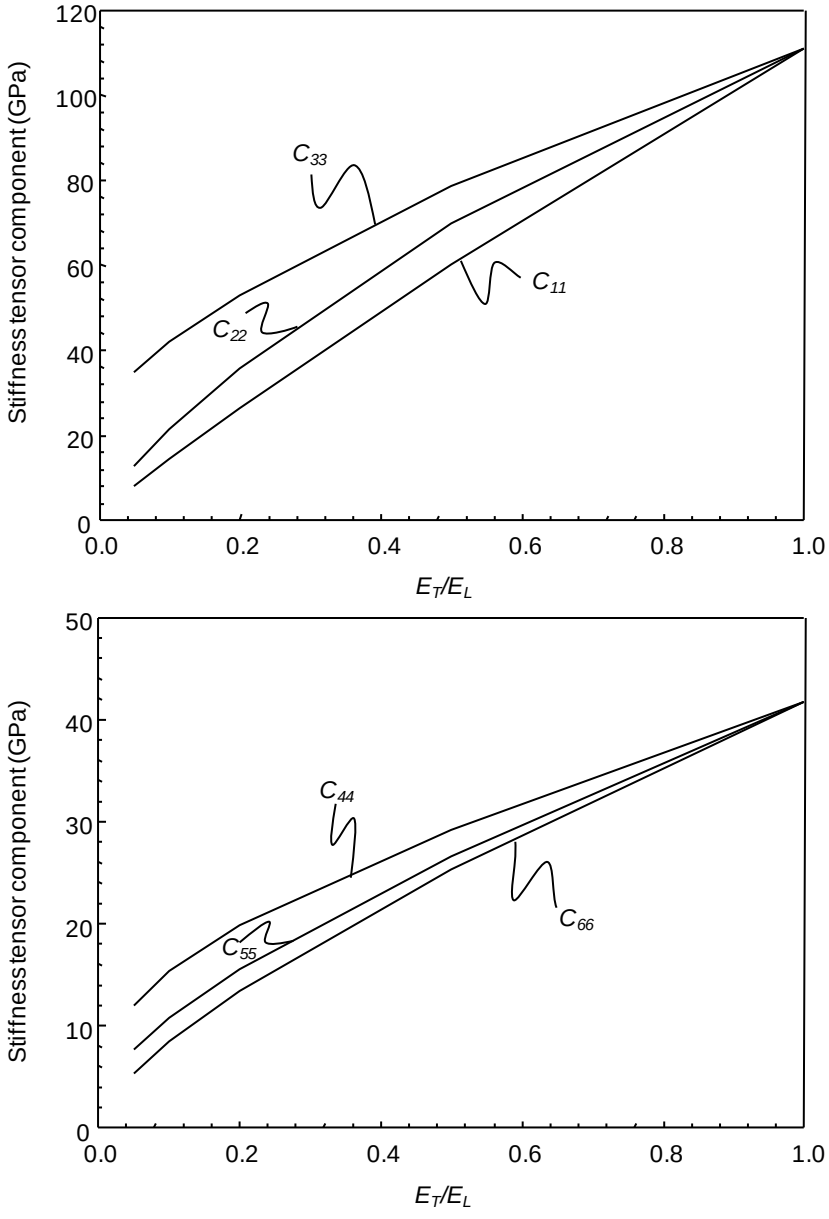

Figure 3.4 Effects of E_T/E_L variation on diagonal components of effective stiffness tensor

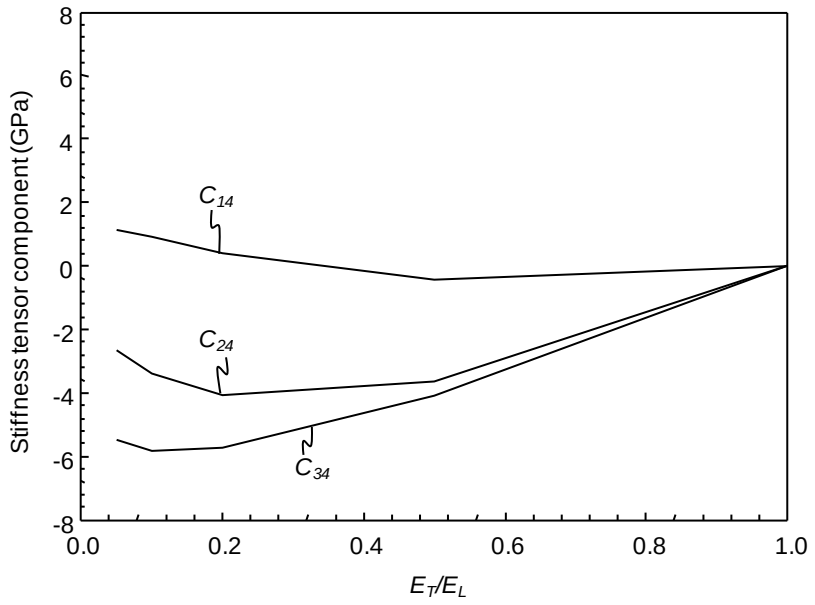

Figure 3.5 Effects of E_T/E_L variation on 3 non-diagonal components of effective stiffness tensor

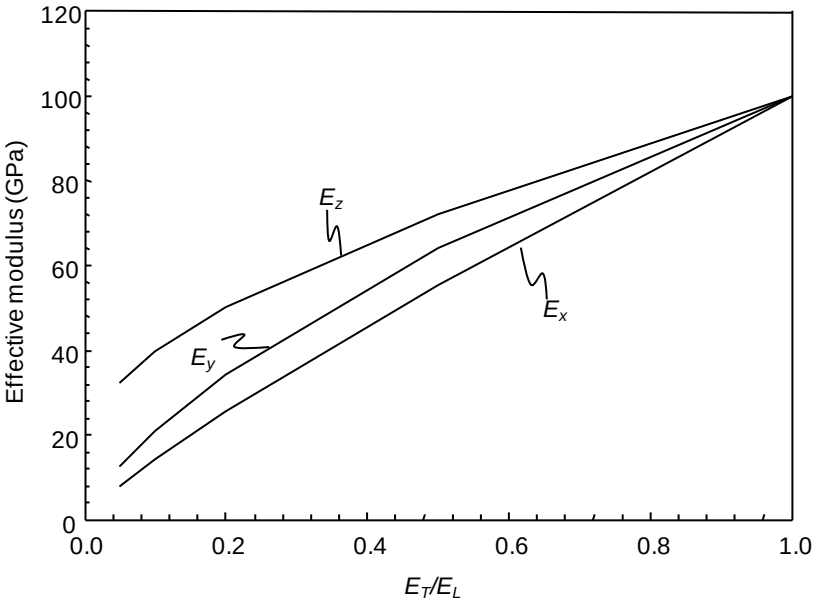

Figure 3.6 Effects of E_T/E_L variation on effective young's moduli

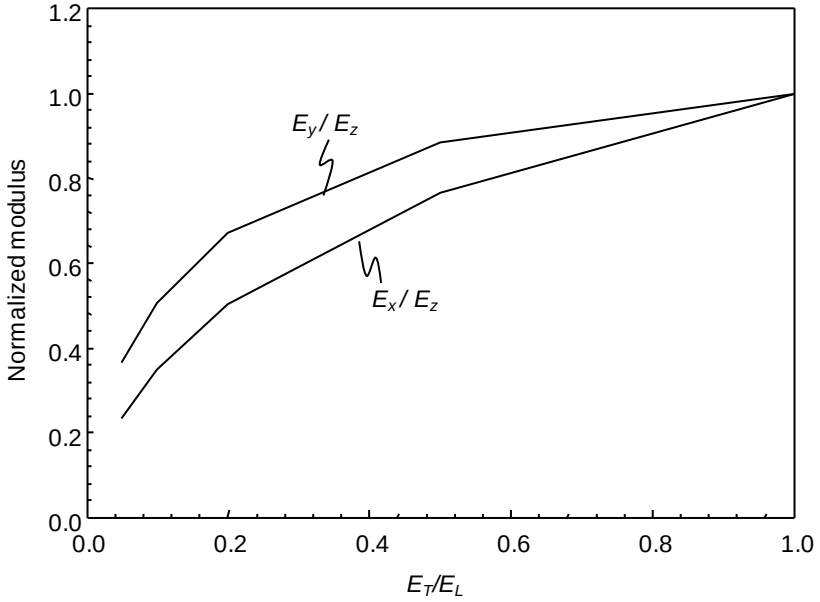

Figure 3.7 Effects of E_T/E_L variation on effective young's moduli normalized by E_z

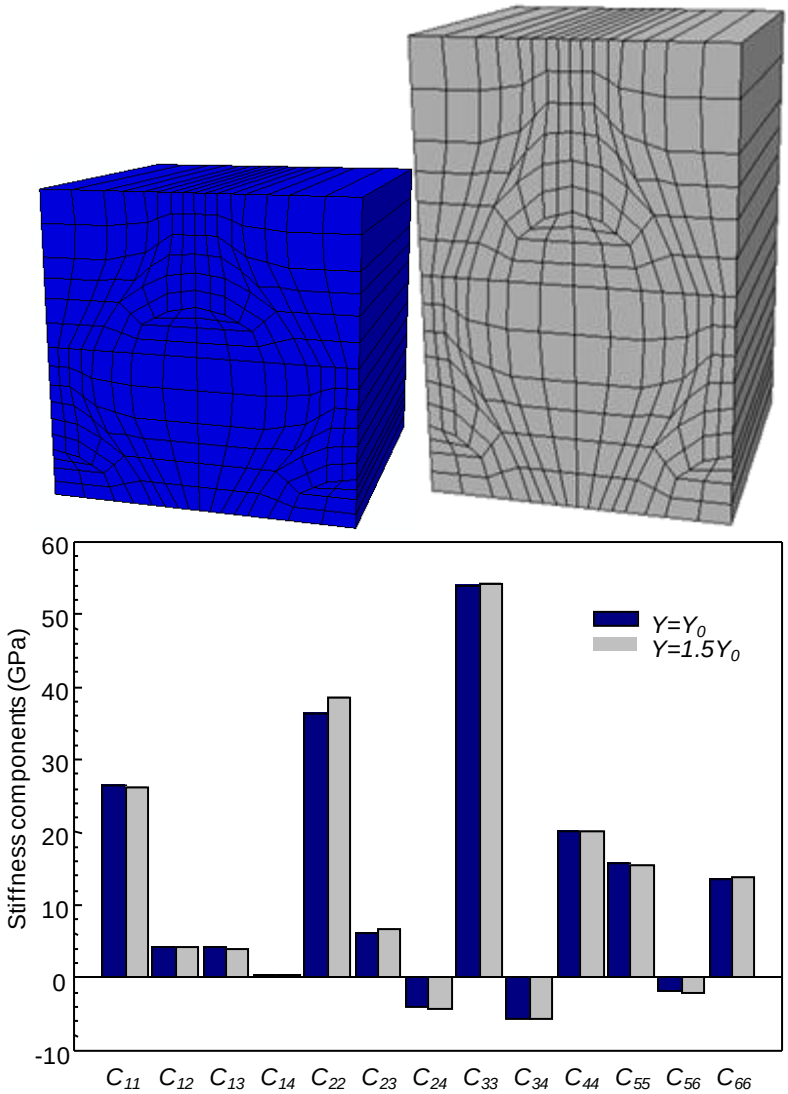

Figure 3.8 Changes of stiffness tensor based on variation of unit cell geometry

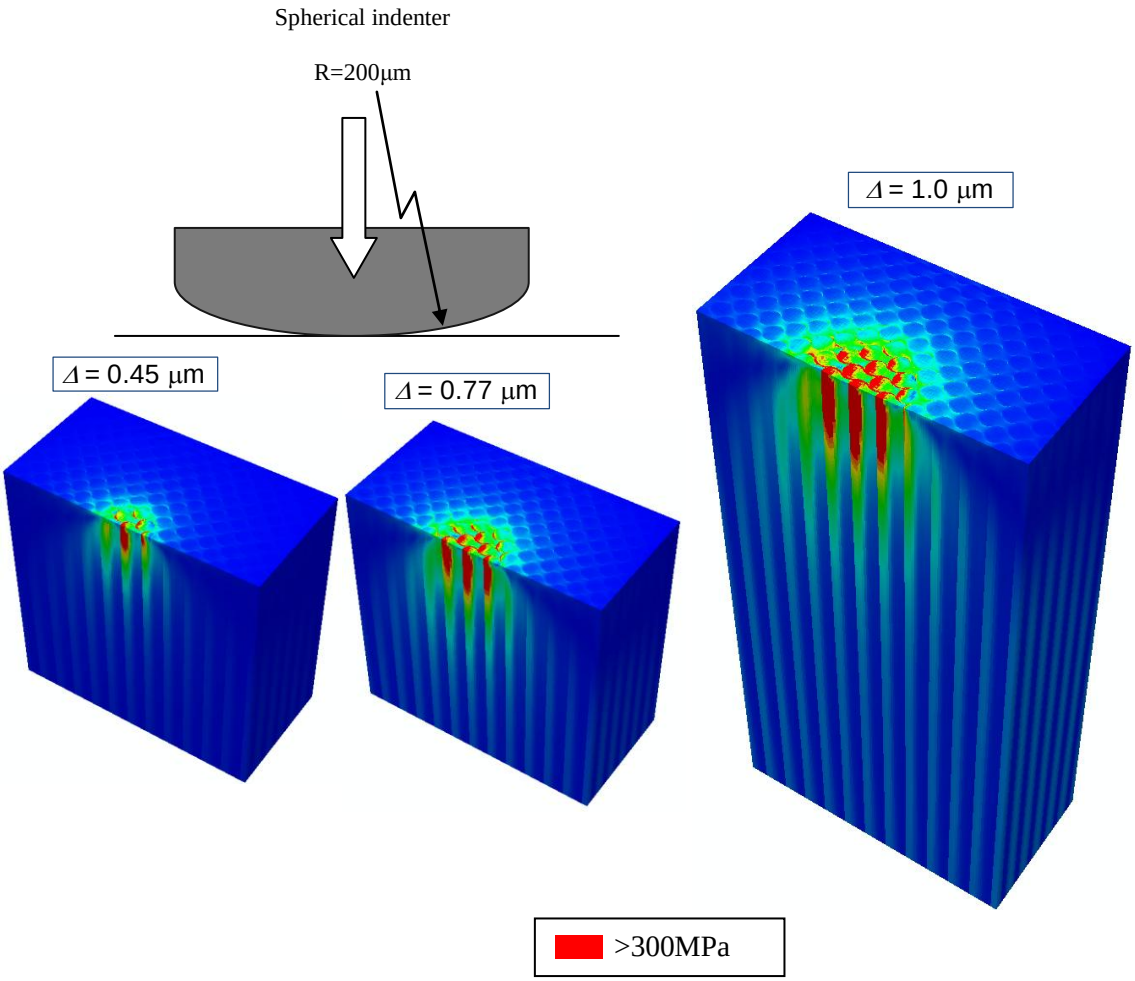

Figure 3.9 Mises stress contour during the indentation for the heterogeneous model with local property ratio of 0.2

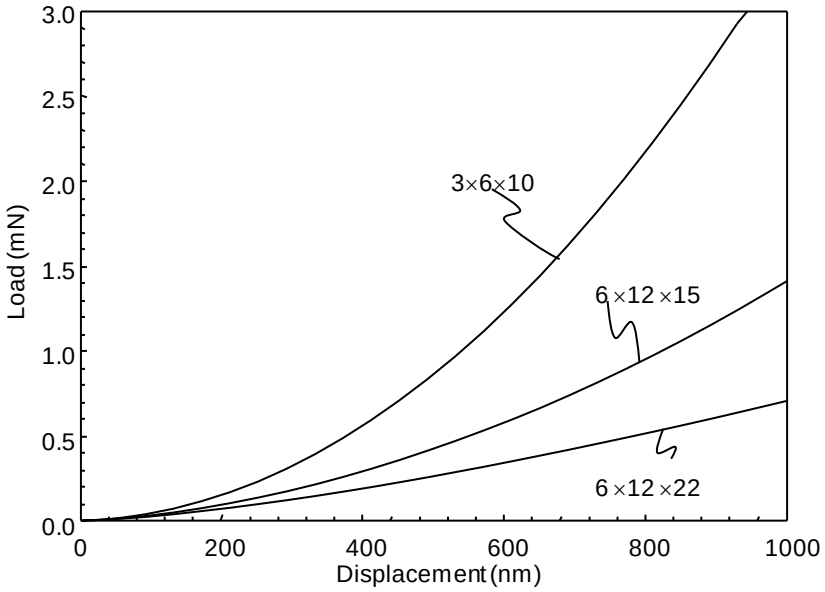

Figure 3.10 Loading curve of enamel with varied model sizes

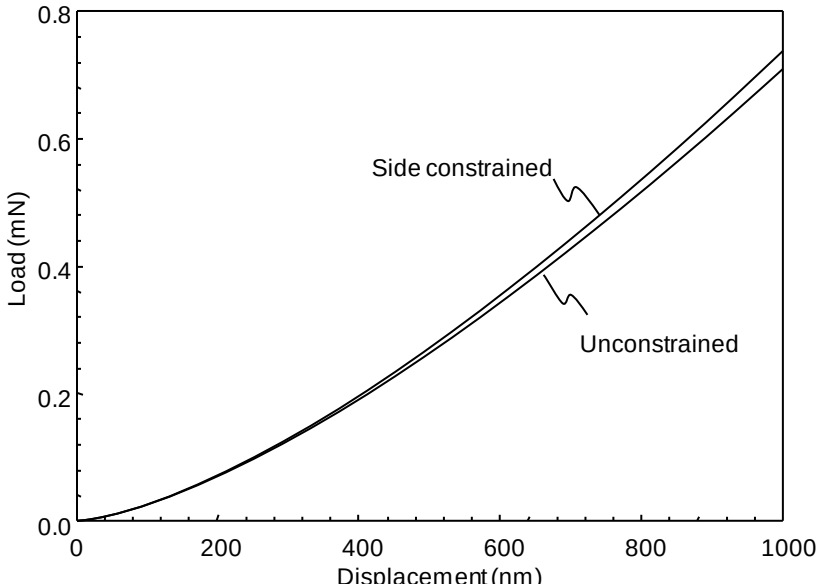

Figure 3.11 Loading curves of 6×12×22 model with side constraining effects

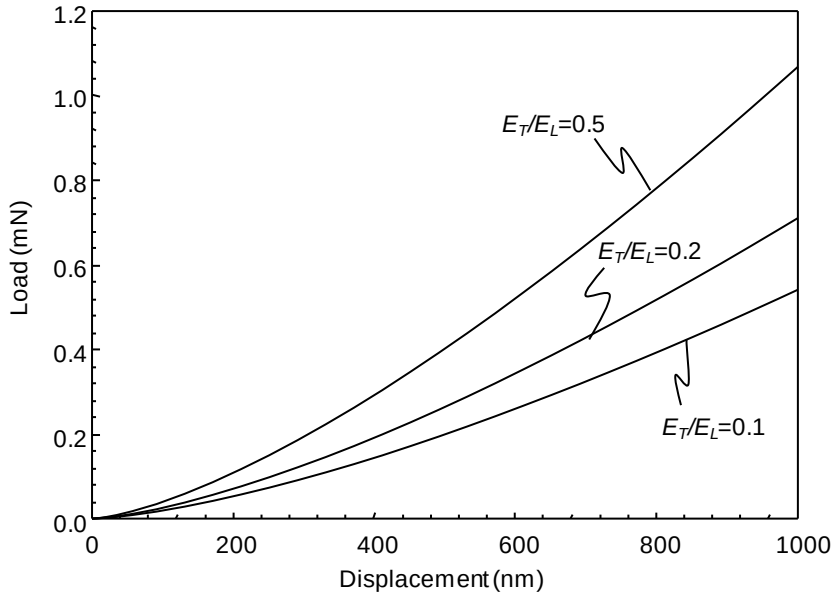

Figure 3.12 Loading curves of enamel with varied local propery ratios

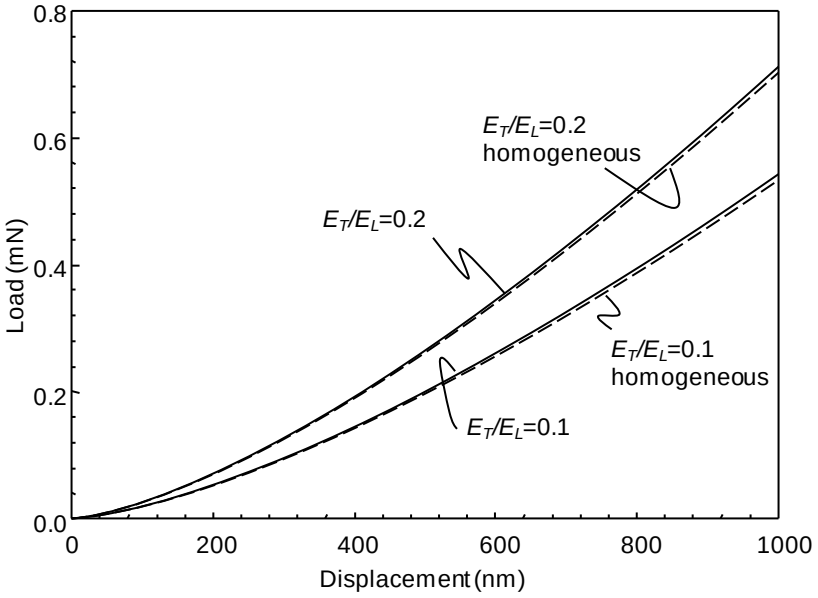

Figure 3.13 Comparison of loading curves between heterogeneous and effective homogenous model with E_T/E_L=0.1 & 0.2

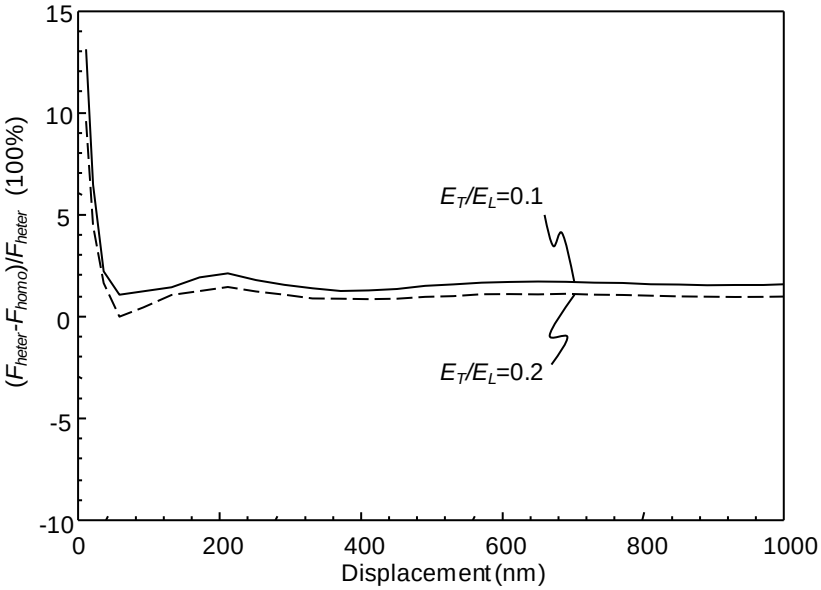

Figure 3.14 Difference of indent forces between heterogeneous and effective homogeneous model with respect to penetration depth

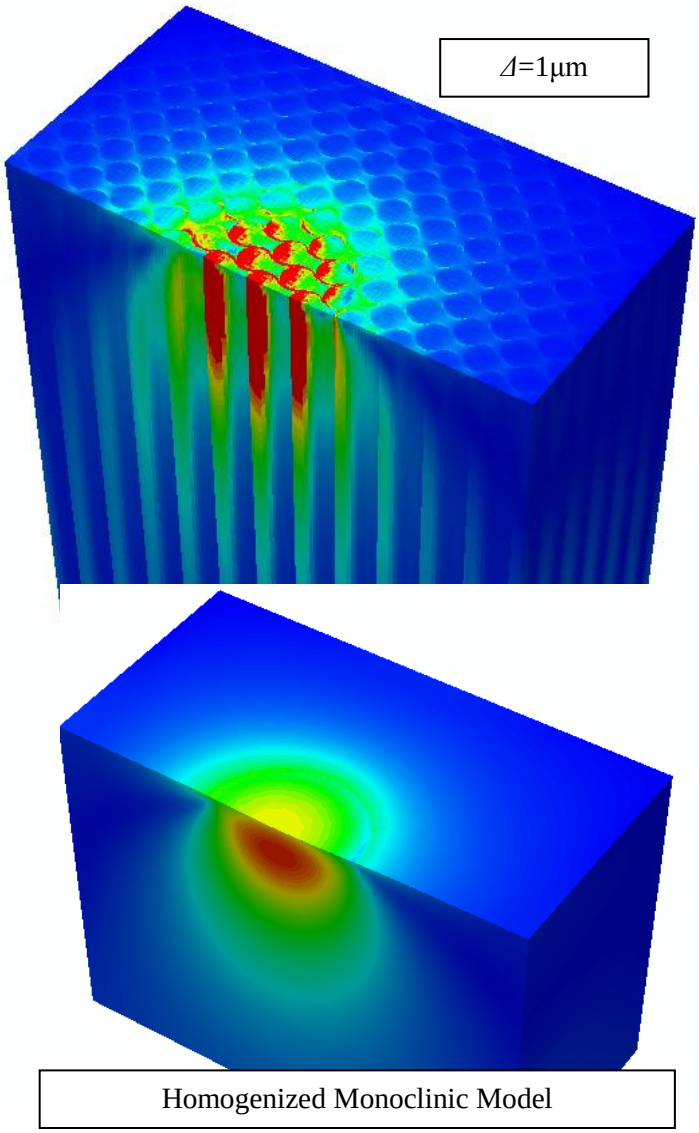

Figure 3.15 Comparison of Mises stress contours of the heterogeneous and homogenized monoclinic models

Chapter 4 Conclusions

This work studies mechanical properties of human tooth enamel based on the complex microstructure through a periodic finite element model.

The main conclusions from the three dimensional finite element model are:

- A representative unit-cell model, which only contains 240 brick elements and is computationally more efficient, was successfully obtained to study the connection between microstructure and the macroscopic mechanical behavior.
- A methodology for applying three dimensional unit-cell periodic boundary conditions (PBC) was utilized in the enamel model.
- Effects of local property variations on the global mechanical properties showed that the effective moduli E_z, E_y and E_x drop 70%, 88% and 92% respectively as the local property ratio E_T/E_L decreases from 1 to 0.05.
- The monoclinic nature of the enamel microstructure was revealed and the constitutive law was calculated with 13 independent material constants for the effective stiffness tensor. C_{11}, C_{22} and C_{33} were the most significant constants, representing the three normal directions. The calculated values fell into the range of the experimental data from microindentation.

Simulations of displacement controlled spherical microindentation were conducted on the bulk model with the same microstructure as the representative unit cell model. The conclusions are:

- Effects of model size on the loading responses showed that as the size increases, the loading forces decrease from over 3 mN to approximately 0.7 mN. At the

model size of 6×12×22, the loading curves became constant and the boundary effects were eliminated.

- The effective modulus in the indentation direction decreased by ~70% as the local transverse modulus decreased from 100 GPa to 5 GPa while the local longitudinal modulus was held constant at 100 GPa.
- Effective homogeneous models were established based on the effective stiffness tensors calculated in this work. The effects of homogenization were investigated in the process of indentation.
- Differences in the loading forces between heterogeneous and homogeneous models drops from 10% to 1%, as the penetration height increases. With the increase in contact area, the homogeneous model begins to show a response similar to the heterogeneous model, where a critical indentation depth is observed when the loading force difference between the homogeneous and heterogeneous models become less than 2% at a penetration depth of ~60 nm.
- Stress distributions of the indentation models were compared, showing that the Mises stress is concentrated in the rod head and extends deep into the enamel bulk following the enamel rods for the heterogeneous model. The maximum Mises stress occurred at the depth of 8.47 μm beneath the surface for the heterogeneous model. The corresponding depth of maximum Mises stress was 4.97 μm for the homogeneous model. The homogeneous model had uniformly distributed stresses within the bulk for the same load application, revealing the importance of considering the microstructure for contact problems.

Chapter 5 Future Work

Recommendations for improvement and future research on the enamel microstructure model include:

- The effects of structural component variations could be studied. People who suffer hypomineralization in enamel have less percentage of HAp in enamel. The effects can be studied by varying the local properties of HAp-protein composites.
- The content variations between the rod and sheath region, in terms of volume fraction of HAp and proteins, should be incorporated into the mechanical properties variations. A layer of sheath region can be modeled along ~3/4 of the boundary of the head regions of the rod with softer material properties.
- The contour mesh could be improved by narrowing the width of the tail region in terms of mimicking the actual microscale shape of the enamel rods.
- Microindentation modeling of the enamel model in the transverse direction could be performed to compare directly with experimental observations, and a refined mesh in the contact region can be incorporated to allow for smaller indenter radii which generate higher strains.
- Spatially resolved indentation modeling could be performed to ascertain the effects of position within the enamel microstructure on the loading results. Inclusion of tangential loading forces in the model will allow the analysis of contact conditions with friction which may be applied to study abrasion mechanisms.
- Restorative materials can be modeled as it is filled or attached to the enamel in terms of its effects on the combination of the mechanical behavior of the mixed

structure for different loading conditions. Such work can provide invaluable information on the restorative material properties and attachment techniques.

References

Avery, J. K., P. F. Steele, et al. (2002). Oral development and histology. Stuttgart ; New York, Thieme.

Daculsi, G., J. Menanteau, et al. (1984). "Length and Shape of Enamel Crystals." Calcified Tissue International **36**(5): 550-555.

Fernandes, C. P., P. O. J. Glantz, et al. (2003). "A novel sensor for bite force determinations." Dental Materials **19**(2): 118-126.

Habelitz, S., S. J. Marshall, et al. (2001). "Mechanical properties of human dental enamel on the nanometre scale." Arch Oral Biol **46**(2): 173-183.

Hayasaki, H., A. Okamoto, et al. (2004). "Occlusal contact area of mandibular teeth during lateral excursion." Int J Prosthodont **17**(1): 72-76.

He, L. H., N. Fujisawa, et al. (2006). "Elastic modulus and stress-strain response of human enamel by nano-indentation." Biomaterials **27**(24): 4388-4398.

Jeng, Y. R., T. T. Lin, et al. (2009). "Nanotribological characterization of tooth enamel rod affected by surface treatment." J Biomech **42**(14): 2249-2254.

Jiang, H. D., X. Y. Liu, et al. (2005). "Ordering of self-assembled nanobiominerals in correlation to mechanical properties of hard tissues." Applied Physics Letters **86**(16): 39011-39013.

Katz, J. L. (1985). "The Biophysical and Biomechanical Properties of Bone, Bone-Mineral and Some Synthetic Bone Biomaterials." Bulletin De La Societe Chimique De France(4): 514-518.

Katz, J. L. and K. Ukraincik (1971). "On the anisotropic elastic properties of hydroxyapatite." J Biomech **4**(3): 221-227.

Kerebel, B., G. Daculsi, et al. (1979). "Ultrastructural Studies of Enamel Crystallites." Journal of Dental Research **58**: 844-851.

Meckel, A. H., W. J. Griebstein, et al. (1965). "Structure of mature human dental enamel as observed by electron microscopy." Arch Oral Biol **10**(5): 775-783.

Mottershead, J. E. and C. D. Foster (1991). "On the Treatment of Ill-Conditioning in Spatial Parameter-Estimation from Measured Vibration Data." Mechanical Systems and Signal Processing **5**(2): 139-154.

Nanci, A. and A. R. Ten Cate (2008). Ten Cate's oral histology : development, structure, and function. St. Louis, Mo., Mosby Elsevier.

Norman, T. L., D. Vashishth, et al. (1995). "Fracture toughness of human bone under tension." J Biomech **28**(3): 309-320.

Oliver, W. C. and G. M. Pharr (1992). "An Improved Technique for Determining Hardness and Elastic-Modulus Using Load and Displacement Sensing Indentation Experiments." Journal of Materials Research **7**(6): 1564-1583.

Ramanujam, N. and T. Nakamura (2007). "Estimating surface damage of composite panels with inverse analysis." Journal of Composite Materials **41**(20): 2471-2498.

Shimizu, D., G. A. Macho, et al. (2005). "Effect of prism orientation and loading direction on contact stresses in prismatic enamel of primates: implications for interpreting wear patterns." Am J Phys Anthropol **126**(4): 427-434.

Spears, I. R. (1997). "A three-dimensional finite element model of prismatic enamel: a re-appraisal of the data on the Young's modulus of enamel." Journal of Dental Research **76**(10): 1690-1697.

Viswanath, B., R. Raghavan, et al. (2007). "Mechanical properties and anisotropy in hydroxyapatite single crystals." Scripta Materialia **57**(4): 361-364.

Weiner, S. and H. D. Wagner (1998). "The material bone: Structure mechanical function relations." Annual Review of Materials Science **28**: 271-298.

White, S. N., W. Luo, et al. (2001). "Biological organization of hydroxyapatite crystallites into a fibrous continuum toughens and controls anisotropy in human enamel." Journal of Dental Research **80**(1): 321-326.

Xie, Z., M. V. Swain, et al. (2009). "Structural Integrity of Enamel: Experimental and Modeling." Journal of Dental Research **88**(6): 529-533.

Zhao, W., C. Cao, et al. (2010). Measurement of Structural Variations in Enamel Nanomechanical Properties using Quantitative Atomic Force Acoustic Microscopy. Proceedings of the 2010 SEM Annual Conference and Exposition, June 7-10, 2010, Indianapolis, IN.

Appendix A. The orientation assignment

The orientation assigned to each element was executed by two angles θ and ϕ as shown in Figure 2.5.The values for each element is listed in Table B.1 with the element numbers shown in Figure B.1. The left hand side elements orients mirror to the right hand side elements.

Element #	θ	ϕ	Element #	θ	ϕ
1	180.0	90.0	31	49.9	38.2
2	0.0	90.0	32	49.9	39.3
3	0.0	90.0	33	70.7	37.2
4	0.0	90.0	34	61.1	37.6
5	90.0	51.4	35	53.0	37.4
6	17.3	55.7	36	46.0	36.9
7	13.5	59.3	37	75.6	37.9
8	11.0	62.0	38	63.4	39.1
9	90.0	52.4	39	51.0	39.6
10	28.6	54.7	40	45.0	40.0
11	22.8	56.8	41	90.0	41.0
12	19.7	58.6	42	70.0	42.0
13	90.0	53.1	43	58.0	43.0
14	45.4	54.7	44	45.0	44.0
15	34.3	56.2	45	90.0	45.0
16	27.3	57.3	46	71.7	46.3
17	83.5	46.3	47	62.4	47.8
18	80.3	48.0	48	52.7	49.7
19	60.4	49.3	49	90.0	49.0
20	41.8	49.6	50	77.6	50.3
21	79.4	42.2	51	68.9	51.9
22	69.6	43.4	52	66.1	53.8
23	53.7	43.7	53	90.0	53.0
24	47.8	44.2	54	83.5	54.2
25	76.1	38.8	55	78.4	55.4
26	64.0	39.2	56	75.6	56.8
27	54.5	39.0	57	89.7	57.1
28	49.3	38.9	58	85.0	58.3
29	70.5	37.7	59	89.6	59.4
30	62.6	37.8	60	81.3	61.3

Table A.1 List of two angles as parameters for element orientation assignment

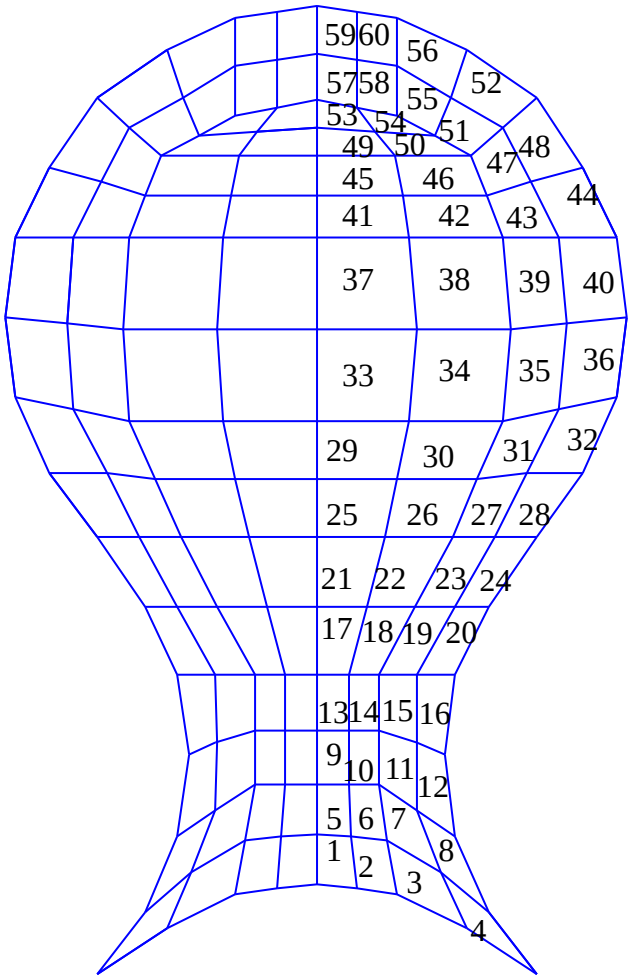

Figure A.1 Element numbering in orientation assignment

Appendix B. Detail calculation on singular value decomposition method

The detail effective stiffness tensor calculation steps using the singular value decomposition method presented in section 2.9 are shown in quantitative pattern for the model with local properties ratio E_T/E_L=0.2. The methodology for models with different local properties ratios is the same.

The collected strain and stress fields under six different loading cases are listed in Table 2.2 and Table 2.3.

After rearrangement of the strain fields, the matrix $\boldsymbol{B}$ is obtained by combining $\boldsymbol{E^1}$ to $\boldsymbol{E^6}$ and presented as follow in Table B.1.

The matrix $\boldsymbol{B}$ is decomposed into three matrices $\boldsymbol{U}$, $\boldsymbol{S}$ and $\boldsymbol{V}$ as shown in Table B.2, Table B.3 and Table B.4. Thus the singular value decomposition of matrix $\boldsymbol{B}$ is completed and $\boldsymbol{C}$ is calculated by $\boldsymbol{C}=\boldsymbol{V}\boldsymbol{S}^{-1}\boldsymbol{U}^{T}\boldsymbol{A}$.

	1	-0.11	-0.07	-0.06	0	0	0	0	0	0	0	0	0
	0	1	0	0	-0.11	-0.07	-0.06	0	0	0	0	0	0
	0	0	1	0	0	-0.11	0	-0.07	-0.06	0	0	0	0
	0	0	0	1	0	0	-0.11	0	-0.07	-0.06	0	0	0
	0	0	0	0	0	0	0	0	0	0	0	0	0
	0	0	0	0	0	0	0	0	0	0	0	0	0
	-0.14	1	-0.08	0.18	0	0	0	0	0	0	0	0	0
	0	-0.14	0	0	1	-0.08	0.18	0	0	0	0	0	0
	0	0	-0.14	0	0	1	0	-0.08	0.18	0	0	0	0
	0	0	0	-0.14	0	0	1	0	-0.08	0.18	0	0	0
	0	0	0	0	0	0	0	0	0	0	0	0	0
	0	0	0	0	0	0	0	0	0	0	0	0	0
	-0.14	-0.12	1	0.27	0	0	0	0	0	0	0	0	0
	0	-0.14	0	0	-0.12	1	0.27	0	0	0	0	0	0
	0	0	-0.14	0	0	-0.12	0	1	0.27	0	0	0	0
	0	0	0	-0.14	0	0	-0.12	0	1	0.27	0	0	0
	0	0	0	0	0	0	0	0	0	0	0	0	0
	0	0	0	0	0	0	0	0	0	0	0	0	0
B=	-0.16	0.54	0.38	1.07	0	0	0	0	0	0	0	0	0
	0	-0.16	0	0	0.54	0.38	1.07	0	0	0	0	0	0
	0	0	-0.16	0	0	0.54	0	0.38	1.07	0	0	0	0
	0	0	0	-0.16	0	0	0.54	0	0.38	1.07	0	0	0
	0	0	0	0	0	0	0	0	0	0	0	0	0
	0	0	0	0	0	0	0	0	0	0	0	0	0
	0.61	-0.11	0.29	0.05	0	0	0	0	0	0	0	0	0
	0	0.61	0	0	-0.11	0.29	0.05	0	0	0	0	0	0
	0	0	0.61	0	0	-0.11	0	0.29	0.05	0	0	0	0
	0	0	0	0.61	0	0	-0.11	0	0.29	0.05	0	0	0
	0	0	0	0	0	0	0	0	0	0	-1.10	-0.15	0
	0	0	0	0	0	0	0	0	0	0	0	-1.10	-0.15
	0.51	0.37	-0.07	0.04	0	0	0	0	0	0	0	0	0
	0	0.51	0	0	0.37	-0.07	0.04	0	0	0	0	0	0
	0	0	0.51	0	0	0.37	0	-0.07	0.04	0	0	0	0
	0	0	0	0.51	0	0	0.37	0	-0.07	0.04	0	0	0
	0	0	0	0	0	0	0	0	0	0	-0.13	-1.12	0
	0	0	0	0	0	0	0	0	0	0	0	-0.13	-1.12

Table B.1 The rearranged strain matrix ***B*** for the six loading conditions of the unit cell model

	-0.09	0.10	-0.02	0.02	0	-0.03	0.02	-0.75	0.03	0	0	0.00	0.00
	0.24	-0.20	-0.26	-0.26	0	0.16	0.28	-0.05	-0.06	0	0	0.03	0.05
	0.19	-0.03	0.36	0.22	0	0.20	0.31	-0.02	-0.08	0	0	-0.02	0.06
	0.28	-0.20	0.07	0.08	0	-0.22	-0.42	-0.10	0.15	0	0	-0.02	-0.08
	0	0	0	0	0	0	0	0	0	0	0	0	0
	0	0	0	0	0	0	0	0	0	0	0	0	0
	0.24	-0.28	-0.24	-0.30	0	0.10	0.16	0.03	-0.09	0	0	-0.01	0.01
	-0.11	-0.01	0.21	-0.15	0	0.11	-0.28	-0.03	-0.57	0	0	-0.42	-0.29
	-0.21	-0.28	-0.08	0.10	0	-0.42	0.20	0.01	-0.05	0	0	-0.10	-0.24
	-0.23	-0.14	0.27	-0.33	0	0.15	0.02	0.00	0.18	0	0	0.27	0.36
	0	0	0	0	0	0	0	0	0	0	0	0	0
	0	0	0	0	0	0	0	0	0	0	0	0	0
	0.20	-0.12	0.40	0.30	0	0.12	0.17	0.07	-0.05	0	0	0.02	0.01
	-0.24	-0.27	0.08	0.07	0	-0.43	0.22	0.02	0.03	0	0	0.14	-0.19
	-0.07	-0.07	-0.18	0.14	0	0.25	-0.26	-0.02	-0.29	0	0	0.69	-0.32
	-0.18	-0.19	-0.22	0.32	0	0.33	-0.03	0.00	0.05	0	0	-0.33	0.32
	0	0	0	0	0	0	0	0	0	0	0	0	0
	0	0	0	0	0	0	0	0	0	0	0	0	0
U=	0.44	-0.42	0.11	0.01	0	-0.04	-0.20	-0.03	0.08	0	0	-0.01	-0.02
	-0.33	-0.27	0.38	-0.31	0	-0.04	-0.12	-0.02	-0.22	0	0	0.05	0.25
	-0.28	-0.38	-0.29	0.37	0	0.06	-0.08	-0.01	-0.19	0	0	0.02	0.28
	-0.30	-0.24	0.08	-0.08	0	0.46	0.00	0.00	0.52	0	0	-0.15	-0.54
	0	0	0	0	0	0	0	0	0	0	0	0	0
	0	0	0	0	0	0	0	0	0	0	0	0	0
	0.01	0.03	0.12	0.12	0	0.02	0.07	-0.47	0.00	0	0	0.00	0.00
	0.07	-0.22	-0.14	-0.15	0	-0.04	0.26	-0.03	-0.03	0	0	0.06	-0.03
	0.10	-0.04	0.18	0.19	0	0.22	0.12	-0.02	-0.15	0	0	0.22	-0.07
	0.12	-0.19	-0.03	0.16	0	-0.04	-0.29	-0.07	0.11	0	0	-0.12	0.06
	0	0	0	0	-0.23	0	0	0	0	0.58	0.77	0	0
	0	0	0	0	-0.67	0	0	0	0	-0.05	-0.23	0	0
	0.05	-0.06	-0.11	-0.12	0	0.03	0.08	-0.42	-0.03	0	0	-0.01	0.00
	0.09	-0.12	-0.06	-0.21	0	0.13	0.04	-0.04	-0.28	0	0	-0.17	-0.10
	0.01	-0.14	0.17	0.17	0	-0.06	0.27	0.00	-0.07	0	0	-0.05	-0.08
	0.06	-0.17	0.16	-0.10	0	-0.06	-0.23	-0.06	0.16	0	0	0.10	0.12
	0	0	0	0	-0.67	0	0	0	0	0.12	-0.22	0	0
	0	0	0	0	-0.23	0	0	0	0	-0.80	0.55	0	0

Table B.2 The column-orthogonal matrix ***U*** for matrix ***B***

	2.10	0	0	0	0	0	0	0	0	0	0	0	0
	0	1.90	0	0	0	0	0	0	0	0	0	0	0
	0	0	1.82	0	0	0	0	0	0	0	0	0	0
	0	0	0	1.66	0	0	0	0	0	0	0	0	0
	0	0	0	0	1.63	0	0	0	0	0	0	0	0
	0	0	0	0	0	1.51	0	0	0	0	0	0	0
S=	0	0	0	0	0	0	1.40	0	0	0	0	0	0
	0	0	0	0	0	0	0	1.28	0	0	0	0	0
	0	0	0	0	0	0	0	0	1.13	0	0	0	0
	0	0	0	0	0	0	0	0	0	1.12	0	0	0
	0	0	0	0	0	0	0	0	0	0	1.05	0	0
	0	0	0	0	0	0	0	0	0	0	0	1.01	0
	0	0	0	0	0	0	0	0	0	0	0	0	0.63

Table B.3 The diagonal matrix ***S*** for matrix ***B***

	-0.09	0.11	-0.02	0.02	0	-0.02	0.07	-0.99	0.02	0	0	0.00	0.00
	0.44	-0.45	-0.41	-0.47	0	0.22	0.37	-0.07	-0.15	0	0	-0.01	0.01
	0.33	-0.14	0.62	0.42	0	0.28	0.46	-0.03	-0.13	0	0	0.02	0.01
	0.51	-0.45	0.16	0.10	0	-0.27	-0.60	-0.14	0.21	0	0	-0.02	-0.02
	-0.12	-0.06	0.23	-0.22	0	0.11	-0.29	-0.04	-0.69	0	0	-0.48	-0.27
	-0.35	-0.49	-0.01	0.15	0	-0.64	0.35	0.02	-0.10	0	0	0.00	-0.25
V=	-0.40	-0.33	0.47	-0.49	0	0.14	-0.07	-0.03	0.13	0	0	0.29	0.37
	-0.07	-0.10	-0.15	0.18	0	0.24	-0.22	-0.03	-0.34	0	0	0.77	-0.35
	-0.30	-0.41	-0.33	0.49	0	0.37	-0.13	-0.02	-0.05	0	0	-0.25	0.42
	-0.20	-0.18	0.04	-0.04	0	0.41	0.00	0.00	0.54	0	0	-0.20	-0.65
	0	0	0	0	0.21	0	0	0	0	-0.59	-0.78	0	0
	0	0	0	0	0.95	0	0	0	0	-0.05	0.30	0	0
	0	0	0	0	0.22	0	0	0	0	0.81	-0.55	0	0

Table B.4 The square orthogonal matrix ***V*** for matrix ***B***